This is the Pre-Published Version.

This is the peer reviewed version of the following article: Z. Shi, R. Ma, L. Shan, H. Tu, Q. Li, J. Su, F. Lu, K. Yu, Z. Geng, P. Slezak, Z. Zhou, E. Hu, S. Shi, G. Lan, R. Xie, Artificial Plateletoids Recruit Blood Proteins to Shield Symbiotic Thrombin: a Silk Fibroin/Calcium Interface Medicated Thrombin Generation and Preservation. Small 2025, 21, 2406909, which has been published in final form at https://doi.org/10.1002/smll.202406909. This article may be used for non-commercial purposes in accordance with Wiley Terms and Conditions for Use of Self-Archived Versions. This article may not be enhanced, enriched or otherwise transformed into a derivative work, without express permission from Wiley or by statutory rights under applicable legislation. Copyright notices must not be removed, obscured or modified. The article must be linked to Wiley's version of record on Wiley Online Library and any embedding, framing or otherwise making available the article or pages thereof by third parties from platforms, services and websites other than Wiley Online Library must be prohibited.

Artificial Plateletoids Recruit Blood Proteins to Shield Symbiotic Thrombin: A Silk Fibroin/Calcium Interface Medicated Thrombin Generation and Preservation

Zhenghui Shi [1], Ruiyao Ma [1], Lianqi Shan [1], Hongyu Tu [2], Qing Li [1], Jing Su [3], Fei Lu [1], Kun Yu [1], Zhen Geng [4], Paul Slezak [5], Zhihang Zhou [6], Enling Hu [1, 7, *], Shuo Shi [7, *], Guangqian Lan [1, *], Ruiqi Xie [1, 5, *]

1 State Key Laboratory of Resource Insects, College of Sericulture, Textile and Biomass Sciences, Southwest University, Chongqing 400715, China

2 Chongqing Customs Technology Center, Chongqing 400044, China

3 College of Textile Science and Engineering, Jiangnan University, Wuxi 214122, China

4 Institute of Translational Medicine, Organoid Research Center, National Center for Translational Medicine (Shanghai) SHU Branch, Shanghai University, Shanghai 200444, China

5 Ludwig Boltzmann Institute for Traumatology, AUVA Research Center, Vienna, 1200, Austria

6 Department of Gastroenterology, The Second Affiliated Hospital of Chongqing Medical University, Chongqing 400010, China

7 School of Fashion and Textiles, The Hong Kong Polytechnic University, Hong Kong, China

Corresponding authors:

Enling Hu (enling.allen.hu@connect.polyu.hk);

Shuo Shi (shuo.shi@polyu.edu.hk);

Guangqian Lan (j070218@swu.edu.cn);

Ruiqi Xie (xie.ruiqi@connect.polyu.hk)

Abstract

Breaking the constraints of thrombin during storage and in vivo applications remains challenging because of its low stability and sensitivity to environmental temperature and acidity. Herein, we developed an artificial plateletoid for in situ thrombin generation through a co-incubation approach with plasma in vitro, utilizing a silk fibroin/Ca^{2+} interface, to enhance the activity and stability of the generated thrombin. Notably, the enzymatic activity of the plateletoid thrombin platform was as high as 30 U/g, leading to rapid clotting within 55 s, and it persisted at least 90 days at as high as 37 °C. This considerably lessens the difficulties associated with maintaining the cold chain while storing and shipping thrombin formulations. Additionally, a gastric bleeding model confirmed that the plateletoid platform improved the acid resistance of thrombin by upregulating the pH of the gastric environment (pH 0.8), facilitating oral delivery of thrombin for effective hemorrhage control in the highly acidic stomach conditions. This pioneering study addresses the constraints of thrombin in storage and in vivo applications and may provide a basis for further research on biological storage and delivery approaches.

Keywords: thrombin, stability, plateletoid, blood protein, gastric hemostasis

1 Introduction

Spontaneous hemostasis involves a series of enzymatic reactions that generate thrombin, a crucial component for blood clotting [1]. Known as coagulation Factor IIa (FIIa), thrombin is widely used as a hemostatic agent in clinical settings [2]. However, thrombin is highly sensitive to environmental temperature, pH, and the nature of the carriers. Commercial thrombin typically requires storage at or below 4 ^{o}C to maintain its enzymatic activity. Research has shown that thrombin nanocomplexes lose significant enzymatic activity over time when stored at 25 ^{o}C [3]. Therefore, the best delivery method for thrombin available right now is cold-chain management. However, cold-chain delivery consumes a significant amount of energy, restricting equitable distribution in regions with scarce resources and shifting the responsibility of safe storage and handling onto the consumer. Because of this complexity, the cost of cold-chain management in clinical trials has gone up by almost 20% since 2015 [4]. Additionally, thrombin is severely deactivated in ultra-low pH environments [5], which limits its use in vivo, such as for oral gastric therapy. Furthermore, thrombin may become inactive when loaded onto inappropriate carriers [6]. For example, thrombin loaded on porous materials often undergoes conformational changes that reduce its bioactivity due to excessive adsorption onto the carrier surface [7]. These limitations highlight the need for improved thrombin-delivery platforms to improve its enzymatic activity and stability for effective hemostasis.

In drug delivery, cargos generated in situ on the carrier often exhibit higher bioactivity

compared to those directly loaded onto the carrier [8]. Thus, generating thrombin in situ on carriers might be a more effective approach to preserve its bioactivity. The blood coagulation cascade involves three successive steps: initiation, amplification, and propagation [9]. The prothrombinase complex, comprising coagulation factors Xa (FXa) and Va (FVa), plays a crucial role in thrombin generation [10]. This complex assembles on the phospholipid membrane of platelets in the presence of Ca^{2+}, converting prothrombin into thrombin by cleavage [11]. The prothrombinase complex assembly involves the transbilayer migration of phosphatidylserine (PS) in platelets. PS binds to Ca^{2+} and moves from the inner to the outer side of the phospholipid bilayer, forming a PS/Ca^{2+} structure [12]. This structure then binds to the negatively-charged Gla domain (γ-carboxyglutamic acid) of FXa and the C2 domain of FVa via Ca^{2+} bridging [13].

The Ca^{2+}-bridging effect is crucial for the assembly of the prothrombinase complex and the catalytic generation of thrombin. Inspired by this, preliminary studies have explored the in situ generation of thrombin on zeolites in the presence of Ca^{2+} [14]. Based on these results, the adsorption mechanism and kinetic modeling of FXa in the prothrombinase complex over zeolite were further elucidated [15]. These studies demonstrated that Ca^{2+} is essential for the self-assembly of the prothrombinase complex and the subsequent in situ generation of thrombin.

Unlike absorption of Ca^{2+} on the rigid surface of inorganic minerals, the presence of functional groups in polymers provides more flexible binding sites [16]. These sites

facilitate the binding of Ca^{2+} through electrostatic interactions, van der Waals forces, and hydrogen bonding, which can enhance the bioavailability of Ca^{2+} and accommodate the conformational changes of coagulation factors during adsorption [17]. However, despite these advances, research on biomimetic interfaces that harbor Ca^{2+}, particularly those based on natural polymers, remains limited. Developing natural polymeric interfaces capable of harboring Ca^{2+} could provide a superior biocompatible interface that mimics the PS/Ca^{2+} structure of real platelets for thrombin generation. In this context, an artificial plateletoid that mimics a real platelet and features a polymeric Ca^{2+} -harboring interface could effectively mediate in situ thrombin generation.

Introducing particles into biological fluids often results in the formation of aggregated biomolecules around them, including proteins, lipids, sugars, nucleic acids, and metabolites [18]. Proteins are the primary focus among these biomolecules. Therefore, plateletoids introduced into plasma may spontaneously form a protein corona around them. Since thrombin is highly sensitive to temperature and has a very short shelf life at room temperature, the use of biomolecules can stabilize its conformation and improve its overall stability [19]. For instance, bovine serum albumin coatings can enhance thrombin's stability when loaded onto nanorobots [20] and also leads to protein aggregation on gold nanoparticles (AuNPs) [21]. As serum albumin is a major plasma protein, plateletoid particles introduced into plasma are highly likely to recruit blood proteins, forming a protein corona around their surfaces. When the protein corona coexists with thrombin, it is expected to enhance thrombin's enzymatic activity,

thermal stability, and structural integrity. However, research on the interaction between thrombin and the protein corona is limited. Since both thrombin and protein corona are generated in situ over plateletoids symbiotically, understanding how the protein corona affects thrombin's enzymatic activity and stability is crucial for improving its application.

Inspired by the role of platelets in hemostasis *in vivo*, this study proposes an artificial plateletoid ($CaCO_3$@CSF/Ca^{2+}) designed to induce in situ generation of thrombin, with stable activity against thermal denaturation even at as high as 37 °C and acidic denaturation at as low as pH 0.8. The plateletoid has a core of microparticle-sized $CaCO_3$ and a shell composing chitosan/silk fibroin multilayer (CSF), which features surface-bound Ca^{2+}. This plateletoid, created for an *in vitro* co-culturing process with platelet-poor plasma (Fig. 1A), aims to (1) mimic activated platelets to assemble prothrombinase complexes for thrombin generation, and (2) recruit essential blood proteins to form a protein corona that stabilizes the generated thrombin. To validate this hypothesis, we conducted a comprehensive analysis of thrombin generation on the plateletoid and the composition of the surrounding protein. We also assessed the effect of the protein corona on thrombin's stability at 37 °C. A gastric bleeding model was used to evaluate the hemostatic effectiveness of the plateletoid thrombin delivery platform ($CaCO_3$@CSF/Ca^{2+}-P). The $CaCO_3$@CSF/Ca^{2+}-P aims to regulate the acidity of gastric fluid in the stomach to offer the preferred physiological conditions and deliver protein corona-shielded thrombin with high activity and stability for effective gastric

hemostasis (Fig. 1B).

This study focuses on the development of a unique thrombin delivery platform, which would be quite competitive to reported thrombin delivery system. The thrombin generated in situ in the platform is expected to have ultra-high stability and activity, addressing issues in storage and transportation of thrombin formulation. Additionally, the platform paves the way for oral delivery of thrombin for gastric hemostasis, expanding the application of thrombin in gastric therapies.

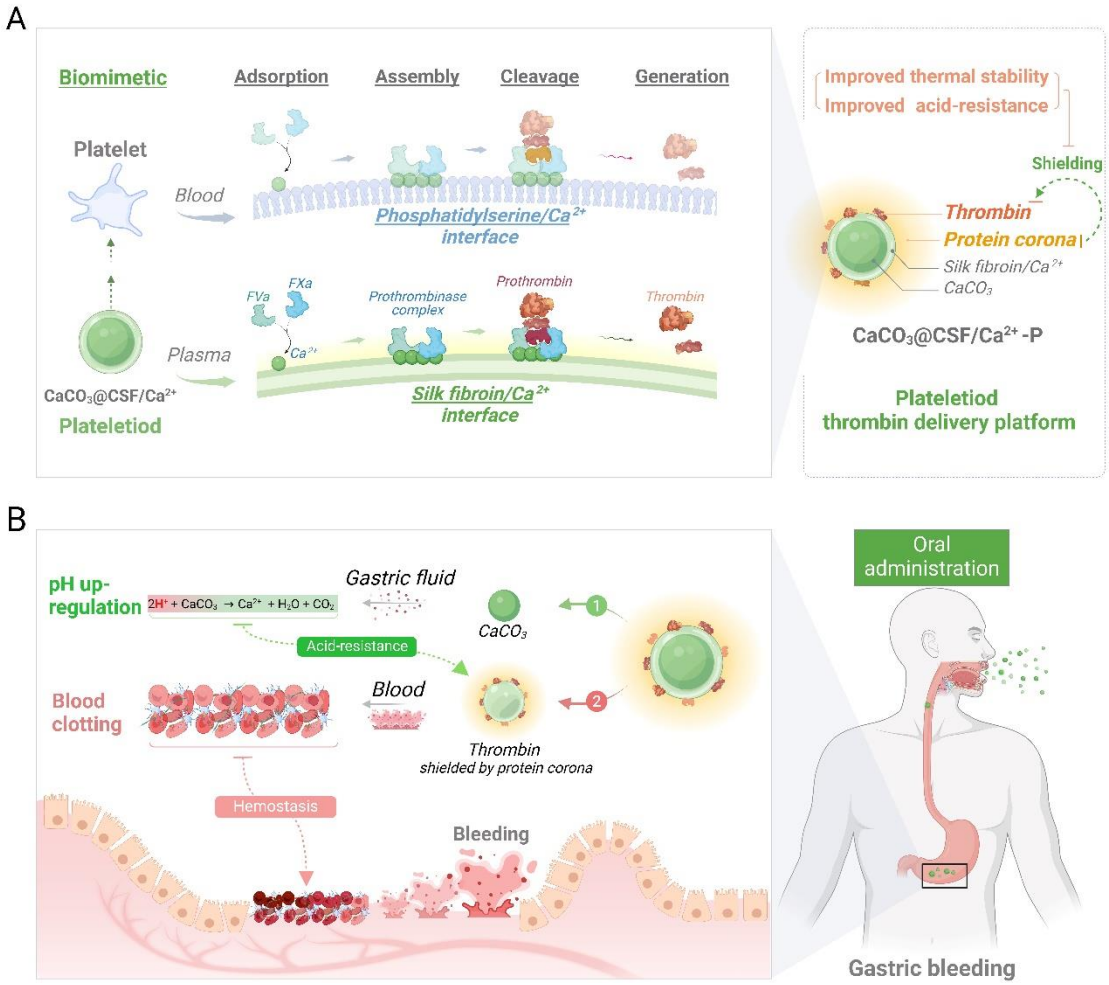

Fig. 1. Action mechanism of the plateletoid ($CaCO_3$@CSF/Ca^{2+}) and the

plateletoid thrombin delivery platform ($CaCO_3$@CSF/Ca^{2+}-P). (**A**) The plateletoid ($CaCO_3$@CSF/Ca^{2+}) induces thrombin generation in situ and recruits blood protein biomolecules from plasma to form a protein corona. (**B**) Hemostatic mechanism of the plateletoid thrombin delivery platform ($CaCO_3$@CSF/Ca^{2+}-P) in gastric hemostasis. (Fig. 1 was created in BioRender. Hu. A. (2023) BioRender.com/t13e817)

2. Results and discussion

2.1 Material design and characterization

In artificial plateletoids, the Ca^{2+}-bridging effect is crucial for the catalytic generation of thrombin from prothrombin in situ. Therefore, creating a biocompatible interface that harbors Ca^{2+} is essential. Key considerations in fabricating the plateletoid include: (1) selecting biocompatible polymers that can bind to Ca^{2+}, (2) choosing an appropriate particle skeleton to immobilize these polymers, and (3) incorporating additional functionalities to facilitate applications in vivo.

The choice of biocompatible polymers is critical, as they ensure the Ca^{2+} bridging effect necessary for thrombin generation in situ. The polymers must bind to Ca^{2+} efficiently. Among the bioactive and biocompatible natural polymers, silk fibroin (SF) stands out due to its rich polar groups, high bioactivity, and structural modifiability. SF has been extensively studied for drug delivery systems and demonstrated their versatility and effectiveness. For instance, SF has been used in template-guided self-weaving technology to develop hyaluronic acid-coated SF carriers for cancer immunotherapy

[22]. Notably, it is capable of binding Ca^{2+} to carbonyl oxygen groups, which weakens hydrogen bonding and hydrophobic interactions between fibrils [23]. Our previous studies have also highlighted the strong interactions between SF and Ca^{2+} [24]. Thus, SF is suitable for creating an SF/Ca^{2+} interface that mimics the natural PS/Ca^{2+} interface found on platelets.

Coating the SF/Ca^{2+} polymer complex onto the surface of the insoluble skeleton provides more reactive sites for thrombin generation. Based on an overview of the particles used in biomaterials, calcium carbonate ($CaCO_3$) is a suitable choice as it can be engineered via template-induced layer-by-layer assembly into porous, hollow, or core–shell structures for drug delivery applications [25]. The introduction of $CaCO_3$ into drug delivery systems for specific applications in vivo has also been extensively investigated in our previous studies [26]. Furthermore, $CaCO_3$ nanoparticles have been shown to enhance the mechanical properties of SF [27], which benefits the robustness of the biomimetic SF/Ca^{2+} interface. $CaCO_3$ can also neutralize gastric fluids, providing additional functionality to establish a favorable physiological environment in the stomach for thrombin stabilization. Therefore, coating SF/Ca^{2+} onto a $CaCO_3$ particle skeleton is a rational approach.

However, the negative zeta potential of $CaCO_3$ particles repels soluble SF polymers. To address this, it is necessary to alter the surface charge of $CaCO_3$ particles to make them positively charged, allowing for the electrostatic adsorption of the negatively

charged SF/Ca^{2+} polymer complex. Chitosan (CS), the only natural cationic polymer among soluble polymers, was used to coat $CaCO_3$ particles, thereby altering their surface potential to positive. This modification provides adsorption sites for the SF/Ca^{2+} complex. After electrostatic deposition of the SF/Ca^{2+} complex onto the $CaCO_3$ particles via CS, the artificial plateletoid with an SF/Ca^{2+} interface is fabricated.

The fabrication process of the artificial plateletoid and the corresponding thrombin delivery platform is illustrated in Fig. 2A. Initially, CS and SF are assembled onto the $CaCO_3$ skeleton layer-by-layer through electrostatic adsorption to form the plateletoid precursor ($CaCO_3$@CSF). Next, $CaCO_3$@CSF is bonded by Ca^{2+} on the surface via robust interaction between SF and Ca^{2+}, resulting in the plateletoid ($CaCO_3$@CSF/Ca^{2+}). When co-cultured with platelet-poor plasma in vitro, the $CaCO_3$@CSF/Ca^{2+} transforms into the plateletoid thrombin delivery platform ($CaCO_3$@CSF/Ca^{2+}-P), which includes a protein corona and carries thrombin with high enzymatic activity and superior room temperature stability for effective hemostasis under harsh physiological conditions.

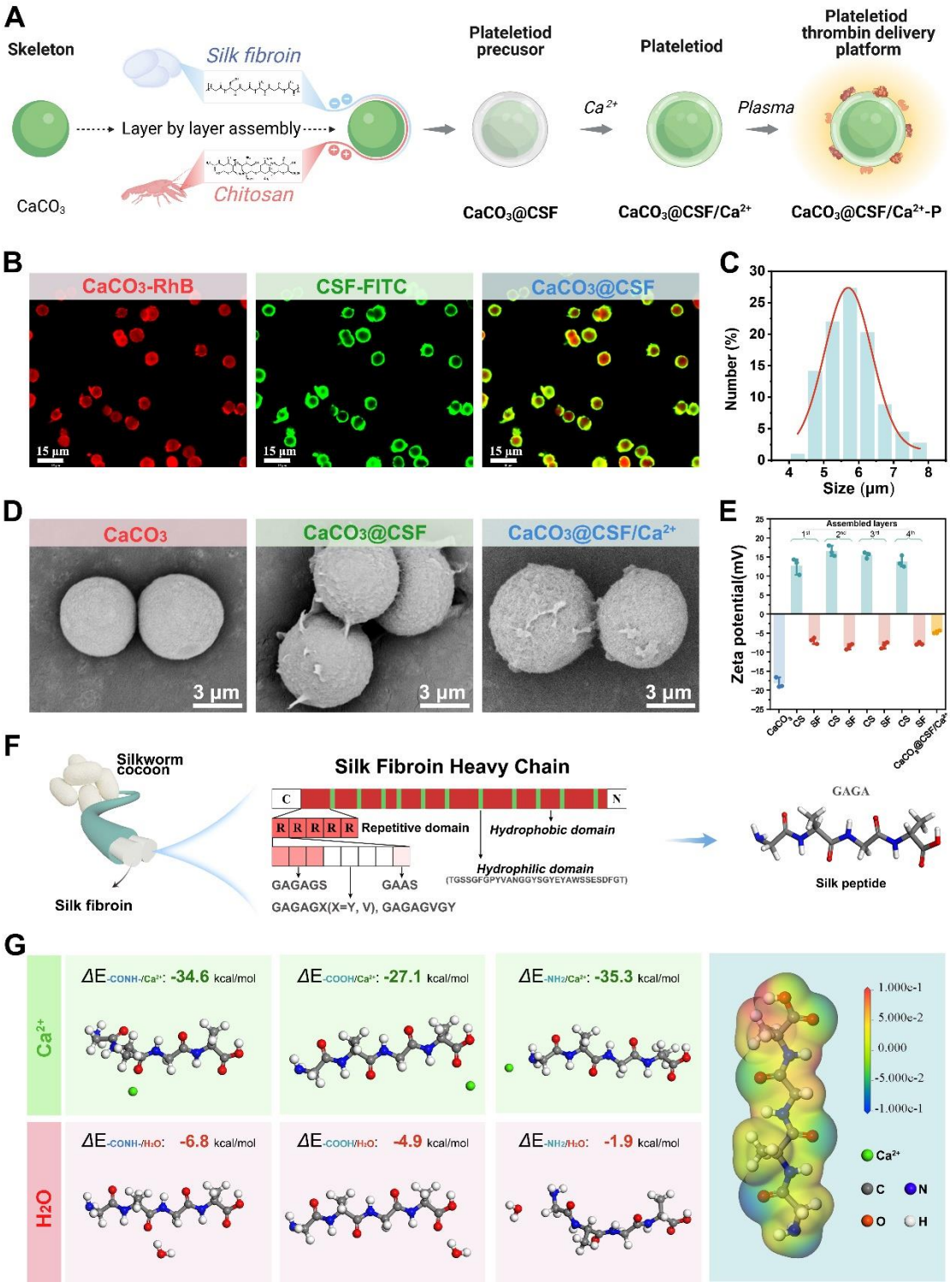

Fig. 2. Fabrication and characterization of the plateletoid materials. (**A**) Preparation of the $CaCO_3$@CSF/Ca^{2+}-P; (**B**) Laser scanning confocal microscopy images of the $CaCO_3$@CSF. The $CaCO_3$ core was stained with rhodamine B (RhB) and the CSF multilayer was stained with fluorescein isothiocyanate (FITC). (**C**) Size

distribution of $CaCO_3$@CSF. (**D**) Scanning electron microscopy images of the $CaCO_3$ skeleton, $CaCO_3$@CSF and $CaCO_3$@CSF/Ca^{2+}. (**E**) Zeta potentials changes during the layer-by-layer assembly in $CaCO_3$@CSF/Ca^{2+} preparation. (**F**) Schematic of the primary structure of SF heavy chain. (**G**) The density functional theory calculations of binding energies between silk fibroin polar groups and Ca^{2+}. (Fig. 2A was created in BioRender. Hu, A. (2024) BioRender.com/o05y729)

Upon fabrication, we performed material characterization of the plateletoid precursor $CaCO_3$@CSF and the final plateletoid $CaCO_3$@CSF/Ca^{2+}. The $CaCO_3$@CSF is a well-defined core-shell sphere with a $CaCO_3$ core and a CSF shell (Fig. 2B and Fig. S1), exhibiting a diameter of 4-8 μm (Fig. 2C), which is comparable to the size of real platelets [28]. Based on clotting time measurements, the optimal number of CS and SF assembly cycles on the surface of $CaCO_3$ was determined to be 4 (Fig. S2). After coating with the CSF shell and binding with Ca^{2+}, the surface roughness of the $CaCO_3$ skeleton increased (Fig. 2D). The increase is due to the alternating assembly of CS and SF polymers over the $CaCO_3$ skeleton for four cycles, which enhances the strength of the SF multilayer for Ca^{2+} binding, with CS applied before SF. Moreover, the $CaCO_3$ skeleton from $CaCO_3$@CSF can be removed using simulated gastric fluid, leaving behind only CSF shells (Fig. S3). This indicates that the CSF shell was successfully wrapped around the $CaCO_3$ core. The successful layer-by-layer deposition of the CSF shell is attributed to the electrostatic adsorption between the positively charged CS and negatively charged SF (Fig. 2E).

In real activated platelets, the PS/Ca^{2+} structure serves as the active site for assembly of the prothrombinase complex assembly [29]. To mimic this, the $CaCO_3$@CSF should have an overall negatively charged surface to firmly bind Ca^{2+}. Because the outermost layer of $CaCO_3$@CSF is an SF polymer, which is negatively charged at neutral pH and contains abundant polar groups [30], it effectively adsorbs Ca^{2+} to form the plateletoid $CaCO_3$@CSF/Ca^{2+}. The firmly bonded Ca^{2+} on $CaCO_3$@CSF/Ca^{2+} promotes the assembly of the prothrombinase complexes for in situ thrombin generation under physiological conditions. Therefore, the negative SF layer(s) on $CaCO_3$@CSF/Ca^{2+} play a critical role in Ca^{2+} immobilization, which is crucial for the prothrombin-to-thrombin conversion process [31]. Although there are no significant morphological changes in $CaCO_3$@CSF or $CaCO_3$ after loading of Ca^{2+} (Fig. 2D for $CaCO_3$@CSF/Ca^{2+} and Fig. S4A for $CaCO_3$/Ca^{2+}), $CaCO_3$@CSF/Ca^{2+} shows an 11-fold higher Ca^{2+} level compared to $CaCO_3$/Ca^{2+} (Fig. S4B). This highlights the importance of SF in effectively binding Ca^{2+} in plateletoids.

Previous research has shown that SF polymers contain multiple domains (Fig. 2F) with polar groups, such as amino (-NH_2), carboxyl (-COOH), and amide groups (-CO-NH-), which interact closely with Zn^{2+} [32]. These polar groups may similarly interact with Ca^{2+}. To investigate this, density functional theory (DFT) calculations were performed to determine the interactions between the SF and Ca^{2+}. Fig. 2G indicates that the electrostatic potential mapping reveals the charge distribution of the protein peptides in

the SF main chain. The binding energies between typical SF polar groups (-CO-NH-, -COOH, and -NH_2) and Ca^{2+} were calculated to be -34.6, -27.1, and -35.3 kcal/mol, respectively, which are significantly lower than those between SF polar groups and H_2O molecules, which are -6.8, -4.9, and -1.9 kcal/mol, respectively. The lower binding energies suggest that SF can bind Ca^{2+} selectively and firmly. Molecular dynamics (MD) simulations were also conducted to explore the interactions between SF and Ca^{2+}. When SF peptides were introduced into a $CaCl_2$ solution, they were surrounded by Ca^{2+} (Fig. S5). The combined DFT calculations and MD simulations confirmed that the SF polar groups on the $CaCO_3$@CSF shell can capture Ca^{2+} electrostatically, forming a robust SF/Ca^{2+} interface that mimics the PS/Ca^{2+} interface of activated platelets for in situ thrombin generation.

2.2 Effective thrombin generation over the plateletoid thrombin delivery platform ($CaCO_3$@CSF/Ca^{2+}-P) in situ

Cargo generated in situ over a drug carrier may have higher bioactivity. Therefore, generating thrombin in situ on plateletoids may better preserve thrombin's bioactivity. Consequently, $CaCO_3$@CSF/Ca^{2+} was introduced into platelet-poor plasma for in situ thrombin loading, resulting in the preparation of $CaCO_3$@CSF/Ca^{2+}-P.

Fig. 3A illustrates the schematic procedure for thrombin generation in situ on $CaCO_3$@CSF/Ca^{2+} to obtain $CaCO_3$@CSF/Ca^{2+}-P, during which blood protein biomolecules may enrich to form a protein corona around the $CaCO_3$@CSF/Ca^{2+}. Fig.

3B shows that $CaCO_3$@CSF/Ca^{2+}-induces flocculation when introduced into platelet-poor plasma for 5.5 min, forming $CaCO_3$@CSF/Ca^{2+}-P. In contrast, $CaCO_3$/Ca^{2+} does not produce insoluble flocs during a 60 min co-incubation with platelet-poor plasma (Fig. S6A). Scanning electron microscopy (SEM) observations confirm that $CaCO_3$@CSF/Ca^{2+} is extensively covered with fibrous biomolecules in the $CaCO_3$@CSF/Ca^{2+}-P sample (Fig. 3C), whereas $CaCO_3$/Ca^{2+}-P remain bare (Fig. S6B). This confirms that $CaCO_3$@CSF/Ca^{2+} recruits blood biomolecules from platelet-poor plasma to cover it with insoluble flocs. Additionally, $CaCO_3$@CSF was also co-incubated with platelet poor plasma to prepare the $CaCO_3$@CSF-P sample. Even after 60 min of incubation, little clots formed in the coincubation bath (Fig. S6C). However, a minimal amount of protein corona was observed over $CaCO_3$@CSF-P (Fig. S6D).

To assess the mass of the insoluble flocs covering $CaCO_3$@CSF/Ca^{2+} in the $CaCO_3$@CSF/Ca^{2+}-P sample, protein concentration in platelet-poor plasma was measured after co-incubation with $CaCO_3$@CSF/Ca^{2+}. Plasma proteins, rich in amino acids such as tryptophan, tyrosine, and phenylalanine, were quantified by measuring absorbance at 254 nm [33]. The absorbance of the $CaCO_3$@CSF/Ca^{2+}-P group was significantly lower than that of the $CaCO_3$/Ca^{2+}-P group (Fig. S7), indicating greater enrichment of blood proteins by $CaCO_3$@CSF/Ca^{2+}. These proteins likely form a protein corona around $CaCO_3$@CSF/Ca^{2+}, enhancing the stability and activity of in situ-loaded thrombin for improved blood clotting. The optimum solid-to-liquid ratio and temperature for incubation of $CaCO_3$@CSF/Ca^{2+}-P were 1:4 (Fig. S8) and 25 °C

(Fig. S9).

Proteomic analysis using liquid chromatography with-tandem mass spectrometry (LC-MS/MS) further identified the protein compositions of the protein corona. Fig. 3D shows that the protein corona in $CaCO_3$@CSF/Ca^{2+}-P is similar to that of platelet-poor plasma, both containing coagulation factors such as serum albumin, immunoglobulins, and fibrinogen. Fig. 3E demonstrates that these factors in platelet-poor plasma and the protein corona surrounding $CaCO_3$@CSF/Ca^{2+} in $CaCO_3$@CSF/Ca^{2+}-P consist of a full set of intrinsic pathway coagulation factors in the cascade. Typically, more than 80% of the coagulation factors from platelet-poor plasma, typically FV/Va, FX/Xa, FXI/XIa, and FXII/XIIa, were extensively recruited by $CaCO_3$@CSF/Ca^{2+} in the $CaCO_3$@CSF/Ca^{2+}-P group (Fig. 3F). Because of the similarity in amino acid sequences and structural properties between active and inactive coagulation factors, it is challenging to distinguish them based solely on their mass-to-charge ratios or fragmentation patterns. Fortunately, in combination with the thrombin activity in $CaCO_3$@CSF/Ca^{2+}-P (Fig. 3I), it is evident that the coagulation cascade reaction is activated, and these coagulation factors are likely to be in their active forms, for example FV and FX are converted to FVa and FXa, respectively. These results demonstrated that the SF/Ca^{2+} interface from $CaCO_3$@CSF/Ca^{2+} led to the accumulation of coagulation factors over $CaCO_3$@CSF/Ca^{2+}-P, promoting the assembly of prothrombinase complexes (FXa and FVa) for in situ thrombin generation.

Thrombin generation from prothrombin is strongly regulated by the membrane-bound prothrombinase complex, composed of FXa and FVa in the presence of Ca^{2+} [34]. Therefore, quantifying FXa and FVa in the protein corona of $CaCO_3$@CSF/Ca^{2+}-P is crucial for assessing its hemostatic performance. As depicted in Fig.s 3G and 3H, significant accumulation of FXa and FVa occurred within the first 4 min, with amounts of FXa and FVa is 30 μg/g and 80 μg/g, respectively in $CaCO_3$@CSF/Ca^{2+}-P, which are substantially higher those in $CaCO_3$/Ca^{2+}-P and $CaCO_3$@CSF-P. Notably, thrombin activity in $CaCO_3$@CSF/Ca^{2+}-P (30 U/g) peaks at 5.5 min during incubation with platelet-poor plasma (Fig. 3I). This increase in thrombin activity confirms that the SF/Ca^{2+} interface of $CaCO_3$@CSF/Ca^{2+} assemble active prothrombinase complexes by enriching FXa and FVa, leading to prothrombin cleavage and thrombin generation. Furthermore, the procoagulant capacity of $CaCO_3$@CSF/Ca^{2+}-P was best at 5.5 min of co-incubation (Fig. S10), which aligns with the thrombin activity results of $CaCO_3$@CSF/Ca^{2+}-P (Fig. 3I). In contrast, $CaCO_3$/Ca^{2+}-P exhibited negligible thrombin activity and minimal effect on clotting time due to the low concentration of Ca^{2+} in $CaCO_3$/Ca^{2+} (1 mg/g) (Fig. S4B), only 10% of that in $CaCO_3$@CSF/Ca^{2+}, which leads to defective blood clotting performance. Additionally, although $CaCO_3$@CSF formed a protein corona incorporating FXa and FVa (Fig. 3G and Fig. 3H), the absence of Ca^{2+} hindered the catalytic transition of prothrombin into thrombin, leading to poor thrombin activity (Fig. 3I) which inhibits fibrin generation and clot formation. These results collectively confirm that the robust binding of SF to Ca^{2+} provides a $CaCO_3$@CSF/Ca^{2+} plateletoid with a strongly active SF/Ca^{2+} interface, which mimics

the real PS/Ca^{2+} interface in platelets, to assemble the prothrombinase complex for in situ thrombin generation.

In summary, the in situ thrombin generation mechanism on the $CaCO_3$@CSF/Ca^{2+} plateletoid is confirmed (Fig. 1A). Initially, $CaCO_3$@CSF/Ca^{2+} activates the intrinsic pathway of blood coagulation by activating FXII, followed by rapid activation of factors such as FX and FV, converting them to FXa and FVa, respectively [35]. The prothrombinase complex is then assembled with FVa (via its C2 domain) and FXa (via its GLA domain) in the presence of Ca^{2+} from $CaCO_3$@CSF/Ca^{2+} [36]. Prothrombin is also linked to $CaCO_3$@CSF/Ca^{2+} (via its GLA domain) [37]. Ultimately, FXa protease residues from the prothrombinase complex, with the FVa's help, cleave prothrombin into thrombin [38], which is then stabilized and protected by the protein corona of $CaCO_3$@CSF/Ca^{2+} -P.

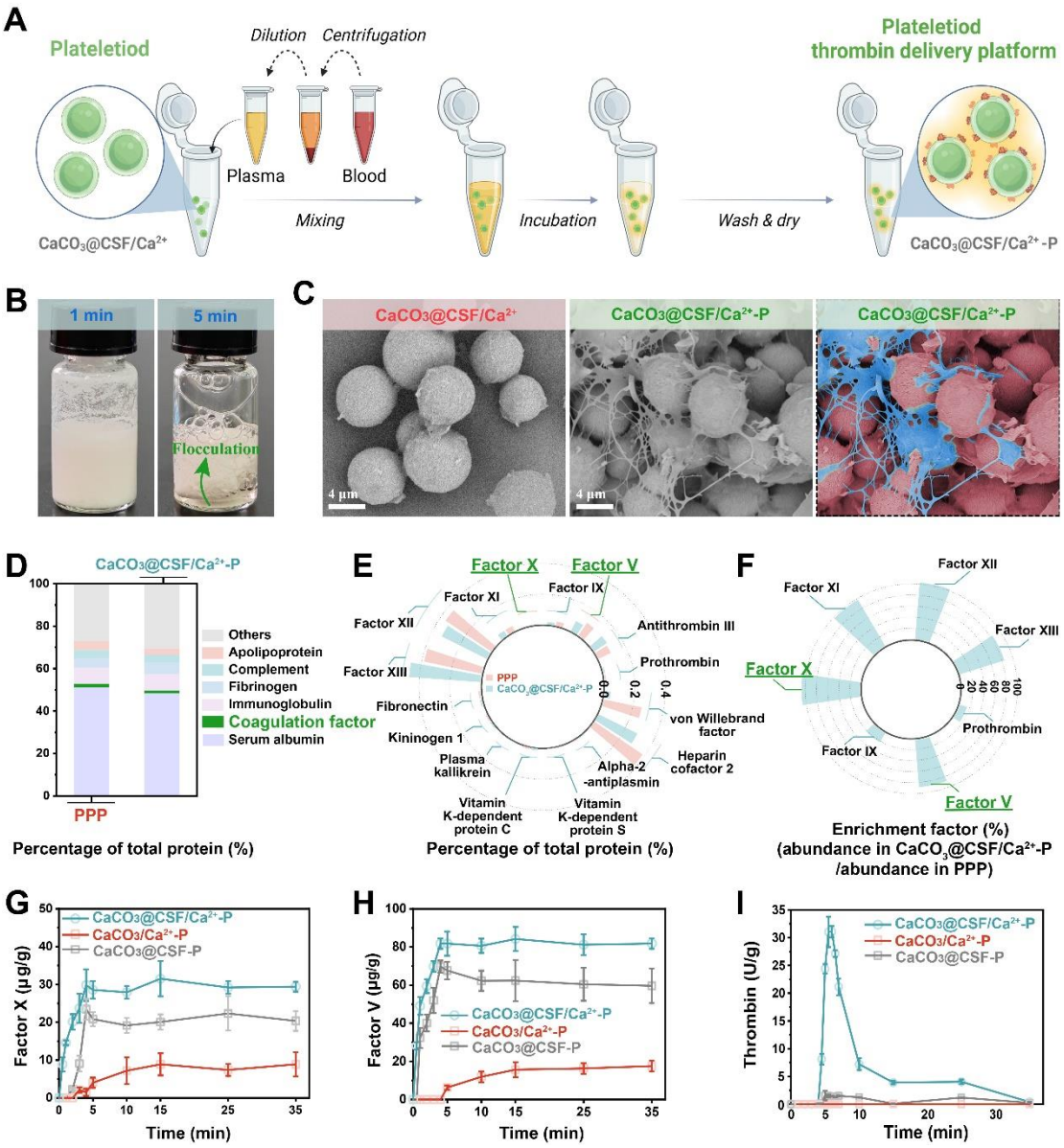

Fig. 3. Characterization of blood protein biomolecules and thrombin induced by the plateletoid ($CaCO_3$@CSF/Ca^{2+}) in the platelet-poor plasma. (**A**) Schematic flow for introducing the plateletoid ($CaCO_3$@CSF/Ca^{2+}) in the platelet-poor plasma to obtain the plateletoid thrombin delivery platform ($CaCO_3$@CSF/Ca^{2+}-P). (**B**) Photos of plateletoid ($CaCO_3$@CSF/Ca^{2+}) dispersion incubated with platelet-poor plasma after 1 min (no flocs) and 5.5 min (flocs formed). (**C**) Scanning electron microscopy images of the plateletoid thrombin delivery platform ($CaCO_3$@CSF/Ca^{2+}-P). (**D**) Proteomic analysis of protein corona in the plateletoid thrombin delivery platform

($CaCO_3$@CSF/Ca^{2+}-P). (**E**) Mass analysis of coagulation factors. (**F**) Enrichment percentages of coagulation factors in the plateletoid thrombin delivery platform ($CaCO_3$@CSF/Ca^{2+}-P). (**G**) Mass of FVa and FXa in the plateletoid thrombin delivery platform ($CaCO_3$@CSF/Ca^{2+}-P). (**H**) Incubation time-dependent thrombin activity of the plateletoid thrombin delivery platform ($CaCO_3$@CSF/Ca^{2+}-P). (Fig. 3A was created in BioRender. Hu, A. (2023) BioRender.com/t13e817)

2.3 Stability of thrombin from the plateletoid thrombin delivery platform ($CaCO_3$@CSF/Ca^{2+}-P)

While the high thrombin activity of the plateletoid thrombin delivery platform ($CaCO_3$@CSF/Ca^{2+}-P) has been confirmed, its stability remains uncertain. Given that commercial thrombin is highly unstable at room temperature and must be stored at or below 4 ^{o}C, assessing the room temperature stability of thrombin from $CaCO_3$@CSF/Ca^{2+}-P is crucial.

Fig. 4A outlines the workflow for evaluating the stability of thrombin from $CaCO_3$@CSF/Ca^{2+}-P at room temperature (37 ^{o}C) over a 90 d period. It was found that the activity of thrombin from $CaCO_3$@CSF/Ca^{2+}-T, prepared by directly loading commercial thrombin onto $CaCO_3$@CSF/Ca^{2+}, decreased significantly over time, with activity completely lost by day 30. In contrast, thrombin from $CaCO_3$@CSF/Ca^{2+}-P remained highly stable, maintaining approximately 30 U/g of activity over 90 d (Fig. 4B). A similar trend in procoagulant activities of $CaCO_3$@CSF/Ca^{2+}-T and

$CaCO_3$@CSF/Ca^{2+}-P is detailed in Fig. 4C. The clotting time in the $CaCO_3$@CSF/Ca^{2+}-T group increased from 55 s to 173 s after 30 days, while the $CaCO_3$@CSF/Ca^{2+}-P group maintained a clotting time of 55 s. This confirms that thrombin loaded onto $CaCO_3$@CSF/Ca^{2+} has low stability at room temperature, whereas $CaCO_3$@CSF/Ca^{2+}-P exhibits superior stability, preserving thrombin's biological enzymatic activity at physiological temperatures and suggesting potential for long-lasting thrombin delivery in vivo. This shall be the longest storage period of thrombin reported ever.

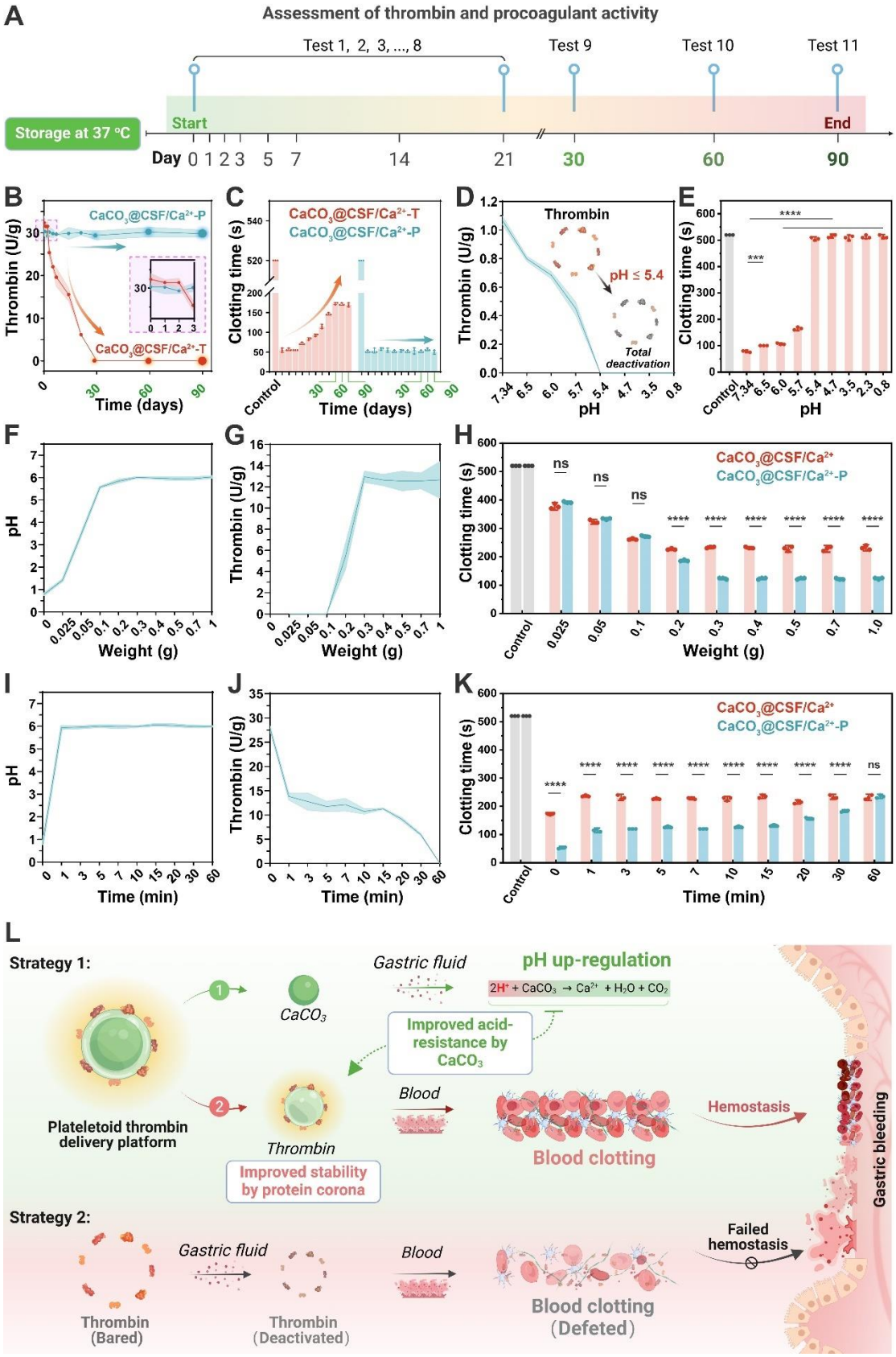

Fig. 4. Thrombin stability of the plateletoid thrombin delivery platform ($CaCO_3$@CSF/Ca^{2+}-P). (**A**) Sampling flow for evaluation of the thrombin activity. (**B**)

Thrombin activity of and (**C**) procoagulant activity of the plateletoid thrombin delivery platform ($CaCO_3$@CSF/Ca^{2+}-P) at 37 °C. Effects of pH on the (**D**) commercial thrombin activity and (**E**) procoagulant activity. (**F**) Effect of the dosage of the plateletoid thrombin delivery platform ($CaCO_3$@CSF/Ca^{2+}-P) on pH of simulated gastric fluids. Effects of the dosage of the plateletoid thrombin delivery platform ($CaCO_3$@CSF/Ca^{2+}-P) on its (**G**) thrombin activity and (**H**) procoagulant activity. (**I**) Effect of time on pH of simulated gastric fluids treated with the plateletoid thrombin delivery platform ($CaCO_3$@CSF/Ca^{2+}-P). Effect of time on (**J**) thrombin activity and (**K**) procoagulant activity of the plateletoid thrombin delivery platform ($CaCO_3$@CSF/Ca^{2+}-P) treated with simulated gastric fluids. (**L**) Schematic actions of the plateletoid thrombin delivery platform ($CaCO_3$@CSF/Ca^{2+}-P) in shielding thrombin for gastric hemostasis. (**** represents $p < 0.0001$, *** represents $p < 0.001$ and ns means no significant difference. Fig. 4A and 4L were created in Biorender. Hu, A. (2024) BioRender.com/m01d167)

The flexibility of thrombin's active site [39] means that prolonged interactions with drug carriers at ambient temperatures can induce conformational changes that lead to irreversible inactivation of thrombin [6]. This may explain the heat-induced inactivation of thrombin in $CaCO_3$@CSF/Ca^{2+}-T. Previous studies suggest that enhancing the rigidity of enzyme active sites through additional interactions can improve enzymatic stability at high temperatures [40]. Therefore, the protein corona from $CaCO_3$@CSF/Ca^{2+}-P, which contains numerous blood proteins, is speculated to induce

extensive interactions with thrombin. These interactions likely increase the rigidity of thrombin's active site, protecting it from heat-induced conformational changes and avoiding irreversible inactivation at room temperature. Thus, the protein corona from $CaCO_3$@CSF/Ca^{2+}-P shields thrombin similarly to a knight's strong shield in battle [41].

In addition to poor room-temperature stability, thrombin's low acidity resistance is a significant barrier to its in vivo applications, such as in gastric bleeding. The low pH of gastric fluid (approximately pH 0.8) rapidly deactivates thrombin [42]. Fig. 4D confirms that commercial thrombin loses its activity completely when exposed to pH ≤ 5.4, with clotting time increasing to 513 s (Fig. 4E). Therefore, assessing the acidity resistance of thrombin from $CaCO_3$@CSF/Ca^{2+}-P is essential for its potential use in the stomach. The thrombin activity of $CaCO_3$@CSF/Ca^{2+}-P was evaluated in simulated gastric fluid. Introduction of various amounts of $CaCO_3$@CSF/Ca^{2+}-P increased the pH of the simulated gastric fluid (Fig. 4F). As the dosage of $CaCO_3$@CSF/Ca^{2+}-P increased, the pH of the simulated gastric fluid rose from 0.8 to 6.0, maintaining thrombin activity at approximately 13 U/g (Fig. 4G). Since $CaCO_3$ from $CaCO_3$@CSF/Ca^{2+}-P reacts with the acidic components in the simulated gastric fluids to generate additional Ca^{2+}, which is known to promote coagulation [43], the coagulation effects of $CaCO_3$@CSF/Ca^{2+}-P (with thrombin) and $CaCO_3$@CSF/Ca^{2+} (without thrombin) are compared in Fig. 4H. After treatment with simulated gastric fluid, $CaCO_3$@CSF/Ca^{2+} showed intermediate clotting time (233 s), which was much longer than that of $CaCO_3$@CSF/Ca^{2+}-P (123 s) and shorter than that of the control (510 s). This suggests that the superior clotting

performance of $CaCO_3$@CSF/Ca^{2+}-P is a combined result of thrombin carried by $CaCO_3$@CSF/Ca^{2+}-P and Ca^{2+} released from $CaCO_3$ in $CaCO_3$@CSF/Ca^{2+}-P.

Dynamic variations in thrombin activity of $CaCO_3$@CSF/Ca^{2+}-P were also analyzed. Notably, $CaCO_3$@CSF/Ca^{2+}-P (0.3 g) rapidly increased the pH of the simulated gastric fluid (10 mL) from 0.8 to 6.0 within 1 min (Fig. 4I). Although thrombin activity decreased significantly due to the initial strong acidity of the stimulated gastric fluid, $CaCO_3$@CSF/Ca^{2+}-P sustained high thrombin activity above 11 U/g for up to 15 min, with a gradual decrease thereafter. The procoagulant efficacy of $CaCO_3$@CSF/Ca^{2+}-P in the simulated gastric fluid was evaluated, showing that within 60 min, the clotting time of $CaCO_3$@CSF/Ca^{2+}-P was significantly lower than that of $CaCO_3$@CSF/Ca^{2+} due to preserved thrombin activity (Fig. 4K). The action mechanism of $CaCO_3$@CSF/Ca^{2+}-P in the simulated gastric fluid is illustrated in Fig. 4L. Initially, $CaCO_3$ from $CaCO_3$@CSF/Ca^{2+}-P neutralizes the acidic gastric fluid, raising the pH to 6.0, which helps maintain thrombin activity and ensures effective procoagulant performance. Additionally, thrombin shielded by the protein corona exhibits superior stability in the gastric environment, contributing to effective hemostasis (Strategy I). In contrast, bare thrombin is deactivated by stimulated gastric fluid, leading to ineffective hemostasis due to defective clotting (Strategy II). These results collectively suggest that (1) $CaCO_3$@CSF/Ca^{2+}-P can increase the pH of simulated gastric fluids to maintain thrombin activity, and (2) the superior procoagulant activity of $CaCO_3$@CSF/Ca^{2+}-P is due to both thrombin it carries and the Ca^{2+} released by $CaCO_3$@CSF/Ca^{2+}-P.

2.4 Hemostatic mechanism

In spontaneous hemostasis, thrombin facilitates (1) the transformation of erythrocytes to echinocytes to release procoagulants, (2) platelet activation to form platelet plugs, and (3) the cleavage of fibrinogen into fibrin meshes to reinforce blood clotting (Fig. 5A). Therefore, the effects of $CaCO_3$@CSF/Ca^{2+}-P on erythrocytes, platelets, and fibrinogen were investigated at the cellular level. As shown in Fig. 5B, $CaCO_3$@CSF/Ca^{2+}-P exhibited substantial erythrocyte adhesion to its surface. The number of adsorbed erythrocytes was similar among $CaCO_3$@CSF/Ca^{2+}-P, $CaCO_3$@CSF/Ca^{2+}, $CaCO_3$@CSF, and $CaCO_3$. However, a significant number of echinocytes, distinct from the typical biconcave disk-shaped erythrocytes (Fig. S11), were observed exclusively on $CaCO_3$@CSF/Ca^{2+}-P. Previous studies have shown that the transition from erythrocytes to echinocytes is linked to the transformation of adenosine triphosphate to adenosine diphosphate, which activates platelets to promote procoagulant release and hypercoagulation [44]. Thus, the transition of erythrocytes to echinocytes indicates the potential of $CaCO_3$@CSF/Ca^{2+}-P to induce coagulation (Fig. 5B).

In addition to the erythrocyte transition, $CaCO_3$@CSF/Ca^{2+}-P also induced the most significant platelet aggregation among all samples (Fig. 5C), resulting in the highest fluorescence intensity of CD41 (Fig. S12). The quantitative analysis of platelets showed that the number of platelets on $CaCO_3$@CSF/Ca^{2+}-P was 7.9×10^6, 2-6 times higher

than on $CaCO_3$, $CaCO_3$@CSF, and $CaCO_3$@CSF/Ca^{2+} (Fig. 5D). Since thrombin binds to receptors on platelets, such as glycoprotein (GP) Ib-IX and protease-activated receptors (PARs), to activate platelet aggregation [45], the platelet aggregation induced by $CaCO_3$@CSF/Ca^{2+}-P is likely due to thrombin generation in situ. These results strongly indicate that $CaCO_3$@CSF/Ca^{2+}-P induces platelet aggregation to accelerate blood coagulation directly.

Furthermore, the impact of $CaCO_3$@CSF/Ca^{2+}-P on fibrinogen levels was investigated. Fig. 5E shows that $CaCO_3$@CSF/Ca^{2+}-P particles clearly display fibrin and fibrinogen, and neither $CaCO_3$ nor $CaCO_3$@CSF exhibited these proteins. The transition from fibrinogen to fibrin was further confirmed by optical density analysis, which showed a significant increase in optical density for the $CaCO_3$@CSF/Ca^{2+}-P group over the incubation period, indicating gradual fibrin generation (Fig. 5F). In contrast, neither $CaCO_3$, $CaCO_3$@CSF, nor $CaCO_3$@CSF/Ca^{2+} showed increased optical density within 30 min. Thrombin cleaves fibrinopeptides A and B from fibrinogen exposing “knobs” that bind to “holes” in the γ- and β-nodules to generate fibrin [46]. Therefore, thrombin in $CaCO_3$@CSF/Ca^{2+}-P is primarily responsible for fibrin generation, highlighting its key role in accelerating coagulation by converting fibrinogen into a fibrin mesh to reinforce blood clots.

Overall, $CaCO_3$@CSF/Ca^{2+}-P induces echinocyte formation, platelet aggregation, and fibrin generation for hemostasis (Fig. 5A), independent of the host’s blood-clotting

509 pathway.

510

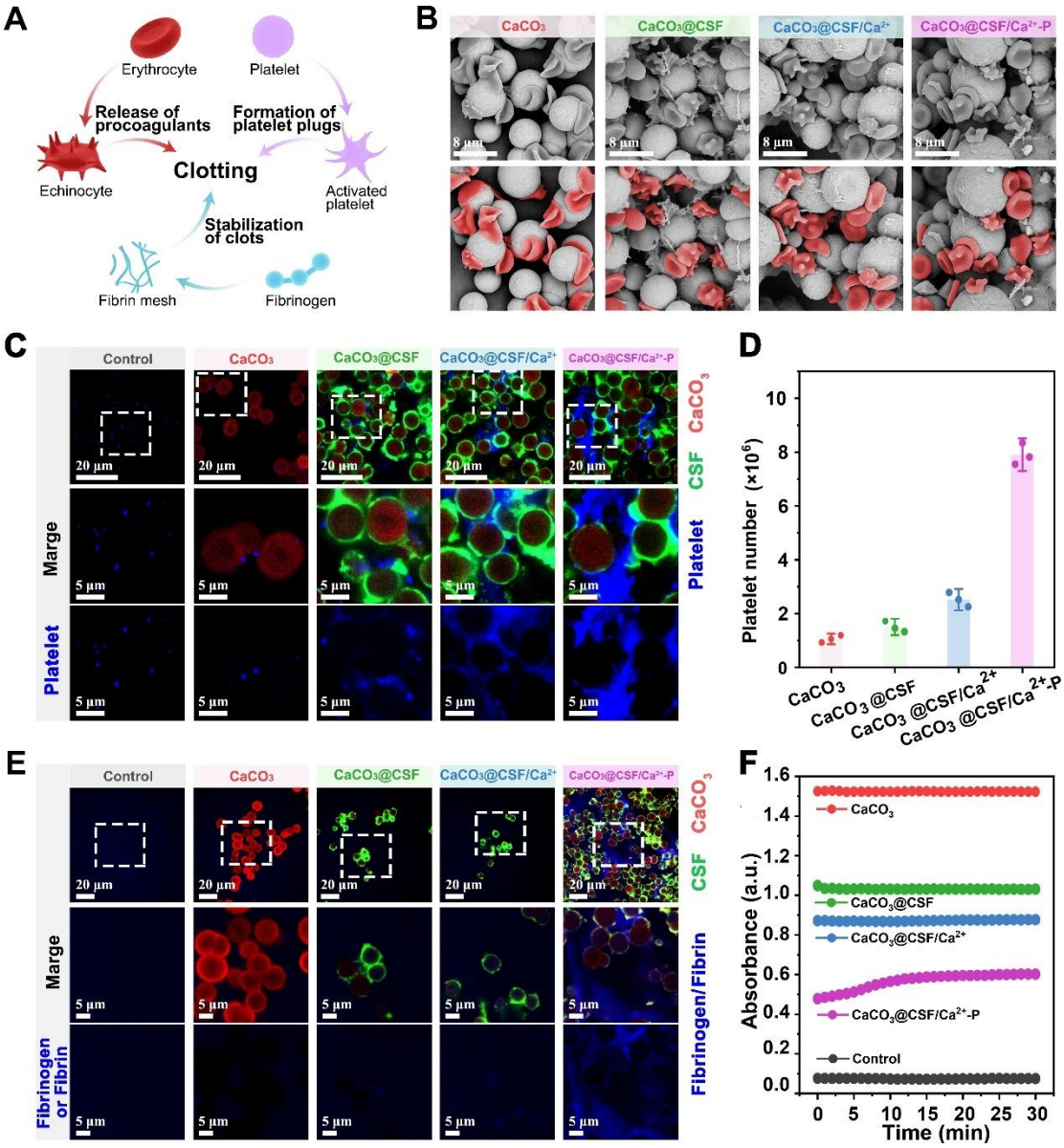

511

512 **Fig. 5. The effect of the plateletoid thrombin delivery platform**

513 **($CaCO_3$@CSF/Ca^{2+}-P) on erythrocytes, platelets, and fibrinogen during**

514 **hemostasis.** (**A**) Schematic mechanism of thrombin in blood clotting. (**B**) Scanning

515 electron microscopy images of erythrocytes transformation. (**C**) Fluorescence images

516 and (**D**) quantitative analysis of platelet aggregation (labeled with CD41a-eFluor 450).

517 (**E**) Fluorescence images and (**F**) quantitative analysis of fibrinogen (labeled with Alexa

518 Fluor 350).

519

520 **2.5 Biosafety evaluation**

521 To address safety concerns, the biocompatibility of $CaCO_3$@CSF/Ca^{2+}-P was evaluated.
522 The hemolysis test, performed at various concentrations of $CaCO_3$@CSF/Ca^{2+}-P,
523 showed a hemolysis ratio of less than 5% across all concentrations (Fig. S13),
524 confirming its excellent hemocompatibility. Additionally, the cytotoxicity of
525 $CaCO_3$@CSF/Ca^{2+}-P was assessed by incubating fibroblast cells with the materials. Fig.
526 6A demonstrates that cell activity in all groups remained above 95% after incubation
527 with $CaCO_3$@CSF/Ca^{2+}-P. The live/dead staining assay further confirmed that
528 $CaCO_3$@CSF/Ca^{2+}-P had a negligible negative influence on the cells (Fig. S14). These
529 results collectively indicate the excellent cytocompatibility of $CaCO_3$@CSF/Ca^{2+}-P.

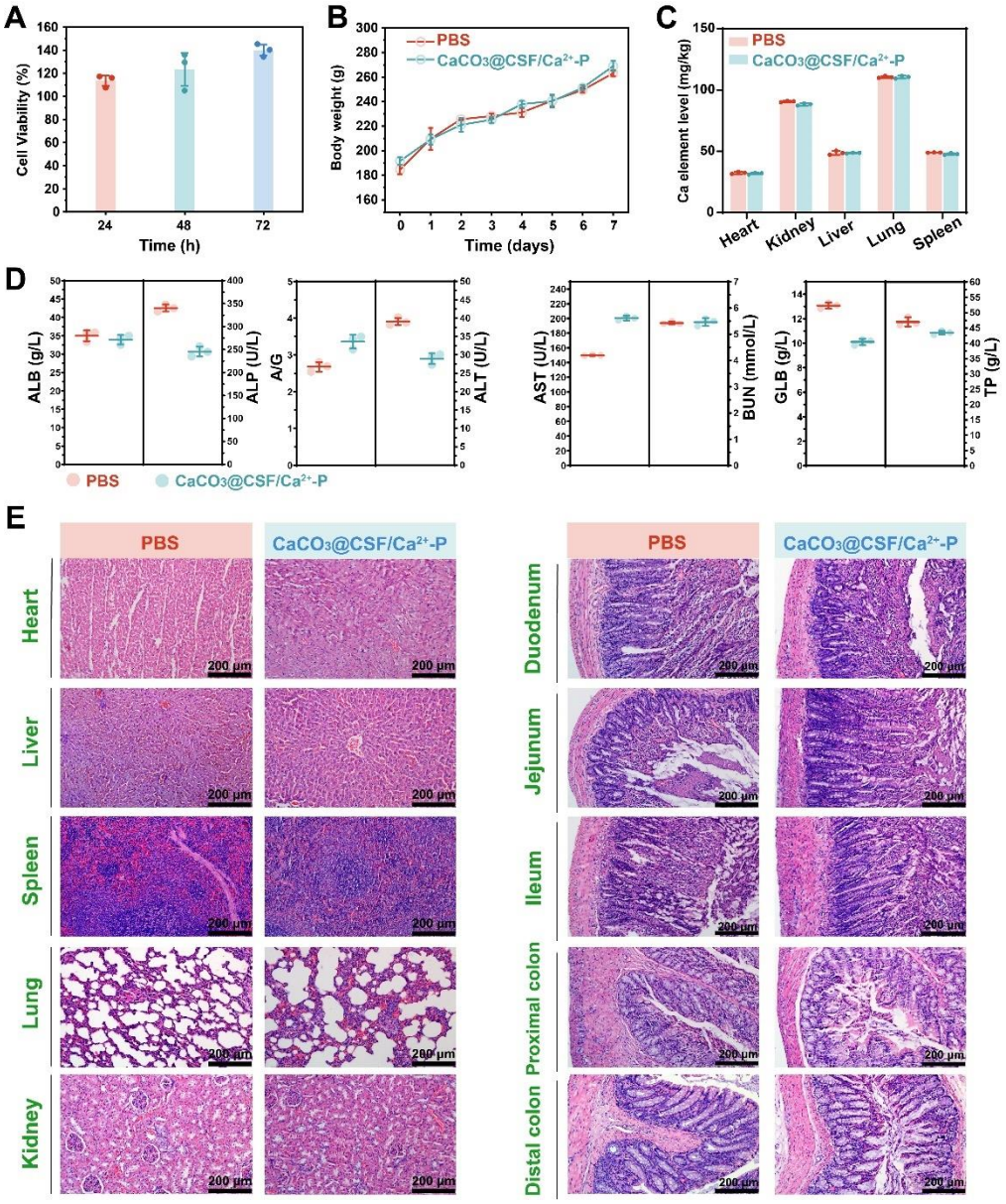

Fig. 6. Biocompatibility and biosafety of the plateletoid thrombin delivery platform ($CaCO_3$@CSF/Ca^{2+}-P). (**A**) Cell viability of fibroblast cells. (**B**) Daily body weight of rats. (**C**) Calcium accumulation in primary organs of rats. (**D**) Blood biochemical indexes of rats. (**E**) Histological staining of gastrointestinal tract and primary organs of rats.

Furthermore, the long-term safety of CaCO3@CSF/Ca2+-P was assessed in vivo using

a rat model. As shown in Fig. 6B, all rats that received oral administration of $CaCO_3$@CSF/Ca^{2+}-P for 7 days showed normal body weight without vomiting or diarrhea. The body weight evolution was comparable to that of the PBS-treated rats, suggesting that $CaCO_3$@CSF/Ca^{2+}-P has minimal impact on rat metabolism. Fig. 6C indicates that calcium accumulation in major organs from the $CaCO_3$@CSF/Ca^{2+}-P group was nearly identical to that in the PBS group. Blood biochemistry was used to evaluate the possible side effects. Markers such as ALT, AST, and ALP can indicate liver health and potential toxicity [47]. Abnormal levels of these markers may suggest liver damage or dysfunction. Parameters like BUN and creatinine levels indicate renal function and potential nephrotoxic effects [48]. Changes in these markers may indicate kidney impairment or toxicity. As there were no significant deviation between the $CaCO_3$@CSF/Ca^{2+}-P group and the control group (Fig. 6D), further signaling no adverse systemic effects of $CaCO_3$@CSF/Ca^{2+}-P on renal and liver functions. Additionally, no visible damage or lesions were observed in the gastrointestinal tract or primary organs (heart, liver, spleen, lung, and kidney) (Fig. S15), which was consistent with the corresponding histological staining assay (Fig. 6E). These results confirm the good biocompatibility and biosafety of $CaCO_3$@CSF/Ca^{2+}-P.

2.6 Treatment of gastric hemorrhage via oral drug delivery

Gastric hemorrhage is a prevalent medical emergency with a mortality rate of approximately 10% [49]. Endoscopic hemostatic treatments, such as mechanical, thermal, and injection devices, are often used as first-line therapies [50]. However, endoscopic

560 hemostasis is limited to hospital settings and depends heavily on the endoscopist's skills
561 [51]. Moreover, these procedures carry risks of thermal damage, perforation, and
562 extensive gastrointestinal necrosis [52]. Therefore, an orally administered formulation
563 for prehospital gastric hemostasis is in high desirable.
564
565 Few studies have explored oral thrombin administration for gastric hemorrhage control,
566 primarily because thrombin is highly unstable under gastric conditions. The acidic
567 environment of the stomach (pH around 0.8) is hostile to thrombin, which quickly loses
568 its hemostatic efficacy [53]. Thus, a formulation that can regulate the gastric environment
569 and maintain thrombin activity is essential. Given the pH upregulation behavior of
570 $CaCO_3$@CSF/Ca^{2+}-P in vitro in stimulated gastric fluid, its therapeutic performance
571 was tested in vivo.
572
573 To begin, the effect of $CaCO_3$@CSF/Ca^{2+}-P on gastric acidity was evaluated.
574 Administration of 30 mg of $CaCO_3$@CSF/Ca^{2+}-P improved the gastric pH 6.5 within 5
575 min (Fig. S16A) and maintained this level for 30 min before gradually returning to
576 normal (Fig. S16B). These results suggest that an appropriate dose of
577 $CaCO_3$@CSF/Ca^{2+}-P can create a more favorable environment for addressing gastric
578 hemorrhage by neutralizing gastric acidity.
579

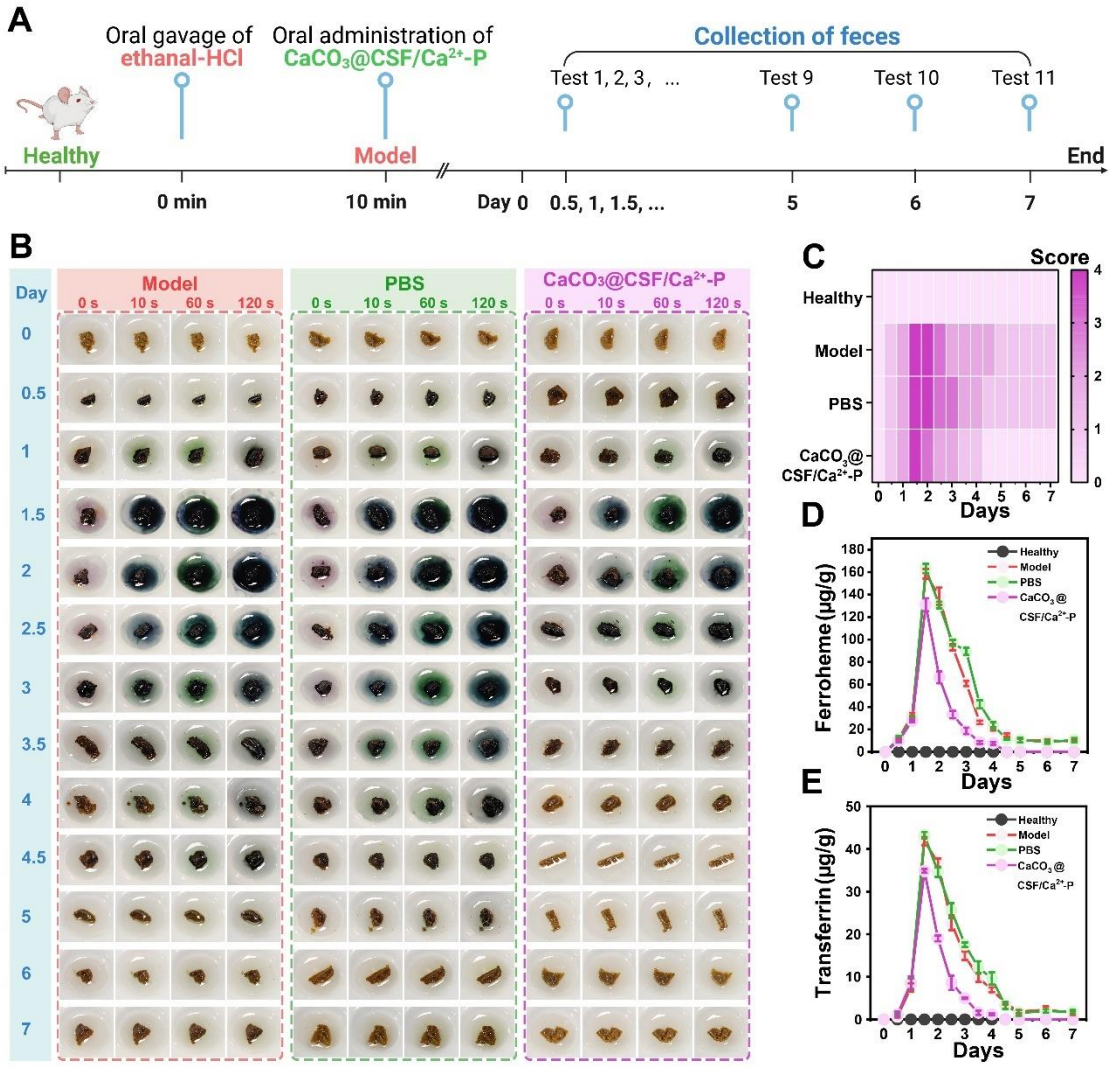

Fig. 7. In vivo hemostatic capacity of plateletoid thrombin delivery platform ($CaCO_3$@CSF/Ca^{2+}-P) in gastric bleeding model. (**A**) Animal experiment flow. (**B**) Rat feces collected from different treatment groups. (**C**) Score of the fecal occult blood test (0 point: no color reaction within 2 min, 1 point: light green changes to green, 2 point: light green changes to bluish brown, 3 point: bluish brown changes to black brown, 4 point: immediately changing to blue-black brown). Quantitative analysis of (**D**) ferroheme and (**E**) transferrin in rat feces. (Fig. 7A was created in BioRender. Hu, A. (2024) BioRender.com/m01d167)

For evaluating the hemostatic potential of $CaCO_3$@CSF/Ca^{2+}-P, an ethanol-HCl mixed solution was used to establish a rat gastric bleeding model. After model establishment, feces were collected for a fecal occult blood assay (Fig. 7A), where the intensity of the color correlates with hemoglobin content. The assay showed no chromogenic reactions in the healthy group (Fig. S17), while reactions were observed in the other groups. Within 7 days, PBS treatment showed negligible therapeutic efficacy, with chromogenic reactions similar to the model group. In contrast, the $CaCO_3$@CSF/Ca^{2+}-P group exhibited a reduction in chromogenic reactions after 1.5 d and complete disappearance after 4.5 d (Fig. 7B). This indicated that $CaCO_3$@CSF/Ca^{2+}-P was the most effective in controlling gastric hemorrhage (Fig. 7C).

Quantitative analysis of ferroheme and transferrin in rat feces further supported the efficacy of $CaCO_3$@CSF/Ca^{2+}-P. The ferroheme content in the $CaCO_3$@CSF/Ca^{2+}-P group (131 μg/g) was significantly lower than in the PBS group (163 μg/g) after 1.5 d (Fig. 7D). Similarly, transferrin content followed the same trend (Fig. 7E). Both ferroheme and transferrin were undetectable in the feces 4.5 d after $CaCO_3$@CSF/Ca^{2+}-P administration, whereas they were still detectable in other groups even after 7 d. These results underscore the superior effectiveness of $CaCO_3$@CSF/Ca^{2+}-P in managing gastric hemorrhage.

Hemostatic efficacy was also assessed through histological and immunofluorescence analyses. Fig. 8A confirms the successful induction of an acute gastric hemorrhage

612 model, with extensive ulceration and congestion observed in gastric tissues after
613 ethanol-HCl gavage. Fluorescence images displayed intense signals distribution in the
614 injured gastric mucosa following oral administration of $CaCO_3$@CSF/Ca^{2+}-P (labeled
615 with FITC onto the CSF component), which was absent in the Model group (Fig. 8B).
616 This indicates that $CaCO_3$@CSF/Ca^{2+}-P adhered to the injured gastric mucosa, a crucial
617 step for effective hemostasis. Fig. 8C shows significant damage to the gastric epithelial
618 barrier and necrosis in the Model group compared to the healthy group. Notably,
619 hemostatic clots were clearly observed on the injured gastric mucosal surface in the
620 $CaCO_3$@CSF/Ca^{2+}-P group, indicating effective incorporation into hemostatic clots. In
621 contrast, the Model and PBS groups showed minimal clot formation. These results
622 unequivocally demonstrate the hemostatic role of $CaCO_3$@CSF/Ca^{2+}-P in gastric
623 hemorrhage.
624

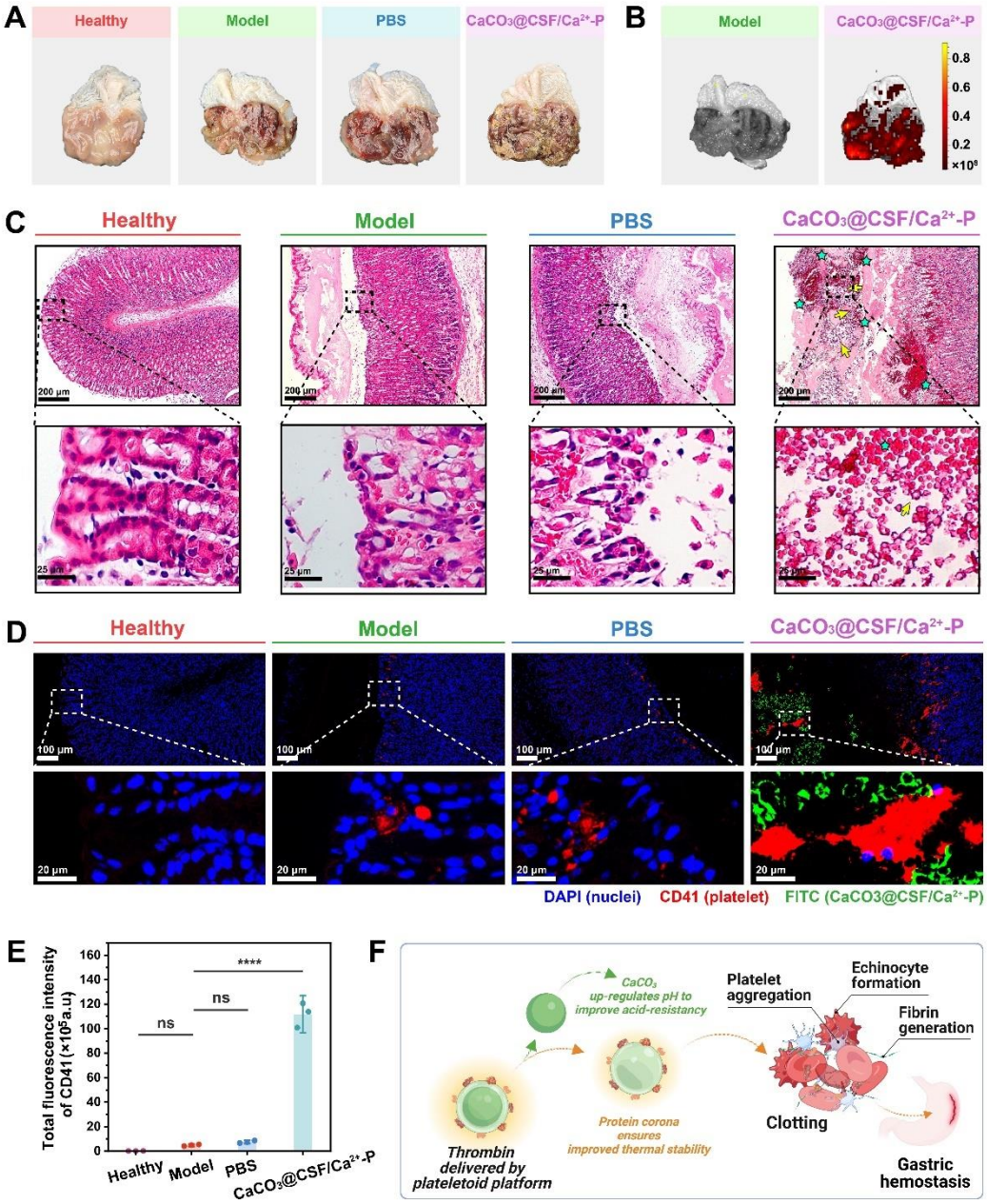

625

626 **Fig. 8. Gastric hemostasis with the plateletoid thrombin delivery platform**
627 **($CaCO_3$@CSF/Ca^{2+}-P).** (**A**) Gastric tissues from bleeding models. (**B**) Fluorescence
628 imaging of the plateletoid thrombin delivery platform ($CaCO_3$@CSF/Ca^{2+}-P) in gastric
629 bleeding tissues. (**C**) Histological staining of the gastric bleeding tissues (hemostatic
630 clots are marked by cyan stars, and the plateletoid thrombin delivery platform
631 ($CaCO_3$@CSF/Ca^{2+}-P) is marked by yellow arrows). (**D**) Immunostainings of platelet

plugs in hemostatic clots of the gastric bleeding tissues. (**E**) Fluorescence intensity of platelet in the immunostaining images. (**F**) Schematic mechanism of plateletoid thrombin delivery platform ($CaCO_3$@CSF/Ca^{2+}-P) in gastric hemostasis. (**** represents $p < 0.0001$ and ns means no significant difference. Fig. 8F was created in Biorender. Hu, A. (2024) BioRender.com/o05y729)

Immunofluorescence staining with CD41 was used to analyze platelet plugs in hemostatic clots. The Model and PBS groups exhibited a limited number of platelet plugs, in contrast to the $CaCO_3$@CSF/Ca^{2+}-P-treated group, which showed a substantial number of platelet plugs co-localized with $CaCO_3$@CSF/Ca^{2+}-P (Fig. 8D). Quantitative analysis demonstrated that the $CaCO_3$@CSF/Ca^{2+}-P group had the highest fluorescence intensity (111.8×10^5), approximately 15-fold higher than the PBS-treated group (7.6×10^5) (Fig. 8E). This indicates that $CaCO_3$@CSF/Ca^{2+}-P significantly enhances platelet plug formation, thereby promoting hemostasis in the injured gastric mucosa.

The hemostatic action of $CaCO_3$@CSF/Ca^{2+}-P in gastric hemorrhage can be attributed to its enhanced acid resistance and thrombin stability. After oral administration, the hemostatic agent adheres to the injured gastric mucosal surface through stomach peristalsis and exerts its effect in a neutral environment, leading to echinocyte formation, platelet aggregation, and fibrin generation for clotting (Fig. 8F).

3. Conclusion

Thrombin's low stability limits its in vivo application due to its sensitivity to environmental temperature, pH, and delivery carriers. This study presents an artificial plateletoid ($CaCO_3$@CSF/Ca^{2+}), with a SF/Ca^{2+} interface mimicking the phosphatidylserine/Ca^{2+} interface of real platelets. During co-incubation with plasma, $CaCO_3$@CSF/Ca^{2+} induces thrombin generation and recruits additional blood proteins to shield the generated thrombin. The thrombin activity of $CaCO_3$@CSF/Ca^{2+}-P remains stable at as high as 37 ºC for at least 90 d, overcoming storage limitations for thrombin formulations. Additionally, $CaCO_3$@CSF/Ca^{2+}-P adjusts the acidity of the gastric environment to enhance thrombin delivery for gastric hemostasis, thus addressing the constraints of oral thrombin administration to highly acidic physiological conditions. This pioneering study focused on the fundamental principles of platelet-induced hemostasis, advancing the field of hemorrhage control. For the first time, it reports an ultra-stable thrombin formulation against thermal and acidic denaturation, while some limitations may raise further research interests. Future works shall focus on the determination of the exact shelf life of the thrombin formulation and the robustness of thrombin activity during real postal service with long-term shipment in a wide temperature range.

4. Experimental

4.1 Materials and chemicals

Bombyx mori cocoons were provided by High Fashion International Limited (Hong

Kong). CS was supplied by Macklin Biochemical Co. Ltd. (Shanghai, China). Commercial thrombin was obtained from Yuanye Biotechnology Co., Ltd. (Shanghai, China). All other reagents were of analytical grade and used as received.

4.2 Animals

All animal experiments adhered to EU Directive 2010/63/EU and were approved by the Animal Experiments Ethics Committee of Southwest University (approval number: IACUC-20240624-01). Male Sprague-Dwley (SD) rats were purchased from Hunan SJA Laboratory Animal Co., Ltd. (China).

4.3 Fabrication of the plateletoid thrombin delivery platform ($CaCO_3$@CSF/Ca^{2+}-P)

Regenerated SF: SF was regenerated [24b], and re-dissolved to a predetermined concentration for use.

Fluorescein isothiocyanate (FITC) labeled CS (FITC-CS): CS (0.5 g) was dissolved in acetic acid (0.1 M) and mixed with methanol. FITC methanol solution (2 mg/mL) was added, and the reaction occurred in the dark at room temperature for 3 h. FITC-CS was precipitated with sodium hydroxide (0.2 M), washed with ethanol, re-dissolved in acetic acid solution (0.1 M) for dialysis against DI water in the dark for 3 d, and lyophilized.

Fabrication of the $CaCO_3$ microparticles: The $CaCO_3$ microparticles, as the skeleton of

698 plateletoid was synthesized as described in the literature [54]. Rhodamine B (Rh-B)
699 labeled $CaCO_3$ (Rh-B-$CaCO_3$) was prepared by adding Rh-B to the $CaCl_2$ solution
700 before Na_2CO_3 addition.
701
702 Fabrication of the plateletoid precursor ($CaCO_3$@CSF): A CS/SF (CSF) multilayer was
703 deposited on the $CaCO_3$ skeleton using layer-by-layer (LBL) assembly [55]. Specifically,
704 0.5 mg/mL CS solution (0.1 M sodium chloride [NaCl], pH 5.5) and 1 mg/mL SF
705 solution (0.1 M NaCl, pH 5.5) were prepared in advance. $CaCO_3$ (2 wt%) was immersed
706 in CS solution for 15 min, centrifuged for 1 min at 2,000 rpm, and washed three times
707 with NaCl solution (0.1 M, pH 5.5) before immersion in the SF solution for 15 min,
708 and collected by centrifugation for 1 min at 2,000 rpm. This process was repeated four
709 times, followed by washing three times with DI water and lyophilization to obtain
710 $CaCO_3$@CSF. Alternatively, FITC-CS and Rh-B-$CaCO_3$ were used to prepare FITC
711 labeled $CaCO_3$@CSF (FITC-$CaCO_3$@CSF) and Rh-B labeled $CaCO_3$@CSF (Rh-B-
712 $CaCO_3$@CSF) following the same procedure.
713
714 Fabrication of plateletoid ($CaCO_3$@CSF/Ca^{2+}): $CaCO_3$@CSF particles (50 mg) were
715 incubated in $CaCl_2$ solution (0.6 M) at 37 °C for 3 h, washed with DI water, and freeze-
716 drying. For comparison, the $CaCO_3$ skeleton was treated using the same procedure as
717 that used for loading of Ca^{2+} for preparation to prepare $CaCO_3$/Ca^{2+}. Ca^{2+} levels on the
718 surface were determined using a Calcium Content Assay Kit (G1218F; Grace, China).
719

720 Fabrication of thrombin delivery platform ($CaCO_3$@CSF/Ca^{2+}-P): The platelet poor
721 plasma was obtained by centrifuging porcine blood for 10 min at 3,000 rpm. The
722 platelet poor plasma was kept at -80 ºC until use. Then, $CaCO_3$@CSF/Ca^{2+} (0.1 g) was
723 mixed in diluted platelet poor plasma (400 μL, dilution factor: 2) at 25 ºC for 5.5 min.
724 The resultant precipitants were lyophilized to obtain $CaCO_3$@CSF/Ca^{2+}-P.
725
726 For comparison, platelet-poor plasma was loaded onto $CaCO_3$/Ca^{2+} and $CaCO_3$@CSF
727 may be performed following the same procedure used to prepare the $CaCO_3$/Ca^{2+} and
728 $CaCO_3$@CSF thrombin delivery platform ($CaCO_3$/Ca^{2+}-P and $CaCO_3$@CSF-P).
729
730 For comparison, commercial thrombin on $CaCO_3$@CSF/Ca^{2+} may be performed.
731 Commercial thrombin (125 U/g) was co-incubated with $CaCO_3$@CSF/Ca^{2+} suspension
732 (0.25 g/mL, 4 mL) at 4 ºC for 1 h. The precipitate was washed thrice and freeze-dried
733 to obtain thrombin-loaded $CaCO_3$@CSF/Ca^{2+} ($CaCO_3$@CSF/Ca^{2+}-T). The ultimate
734 thrombin activity of $CaCO_3$@CSF/Ca^{2+}-T was nearly 32 U/g, which was comparable
735 to that of $CaCO_3$@CSF/Ca^{2+}-P.
736
737 **4.4 Characterization**
738 Laser scanning confocal microscopy (LSCM; FV3000RS, Olympus, Japan), scanning
739 electron microscopy (SEM; SU8010, Hitachi, Japan), and fluorescence microscopy
740 (IX73, Olympus, Japan) were used analyze physical structures. Dynamic light
741 scattering equipment (DLS, ZEV360011000, Malvern, UK) was used to measure zeta

potential. ImageJ software was used to perform particle size analysis.

4.5 Density functional theory (DFT) calculation

Binding energies between polar groups of SF (amino, carboxyl, and amide groups) and Ca^{2+} were calculated using DFT with the Dmol3 program in Materials Studio. The binding energies between H_2O molecules and Ca^{2+} were also calculated for comparison. To determine the exchange and correlation terms, Generalized Gradient Approximation (GGA) was utilized as suggested by Perdew, Burke, and Ernzerhof (PBE). The DNP version 3.5 basis set, and DFT semi-core pseudopotential (DSPP) method were employed to effectively treat the core electrons in calcium. Structural symmetry was ignored in all geometry optimizations. A self-consistent field (SCF) procedure was carried out with a total energy convergence threshold of 1×10^{-6} Hartree to guarantee precise electronic convergence. The molecular clusters were subjected to structure optimization and energy calculations before and after combination utilizing the implicit solvent of the COSMO model. The binding energies of the configurations (E_{bind}) were calculated according to Equation (1):

$$E_{bind} = E_{ab} - E_a - E_b \quad (1)$$

Where, E_a, E_b, and E_{ab} denote the energies of A (Ca^{2+} or H_2O molecules), B (SF polar groups), and the complex energy, respectively.

A negative E_{bind} value indicates that interaction between different materials is exothermic. A higher absolute value of the negative E_{bind} suggests more pronounced exothermic interaction and better stability of the mixture.

4.6 Molecular dynamics (MD) simulation

MD simulations were performed using the GROMACS (version 2019.3) with the Dreiding force field. The size of the simulated box was 10×10×10 nm^3 and it had periodic boundary conditions in all three directions. The simulated box contained 60 Ca^{2+}, 120 Cl^-, and 30 SF peptides and was filled with 6,000 H_2O molecules. After optimization by the Dreiding force field, the system was subjected to a molecular dynamics simulation under an NPT ensemble at room temperature and 1 atm for 1,000 ps. The configuration was visualized using the Visual Molecular Dynamics software.

4.7 Component identification of the protein corona

The protein corona (protein biomolecules enriched) formed on $CaCO_3$@CSF/Ca^{2+}-P was analyzed by LC-MS/MS for proteomic analysis.

Sample preparation: $CaCO_3$@CSF/Ca^{2+} (0.1 g) was incubated with human platelet poor plasma from volunteers (400 μL, dilution factor: 2) at 25 °C for 5.5 min to collect flocs. The experiments were approved by the Ethics Committee of The Second Affiliated Hospital of Chongqing Medical University, Chongqing, China (Approval No. 80). For LC-MS/MS analysis, the washed flocs were resuspended in guanidine hydrochloride

786 solution (6 M, 1 mL). Protein extractions were carried out in SDT buffer (4% SDS, 100
787 mM Tris/HCl, 0.1 M DTT, pH 7.6). In accordance with the filter-aided sample
788 preparation (FASP) procedure, an appropriate amount of protein from each sample was
789 subjected to trypsin cleavage. The digested peptides were desalted on C18 cartridges
790 and lyophilized. Finally, they were redissolved in a formic acid solution (0.1%) before
791 further analysis. The components of human platelet-poor plasma were identified using
792 the same procedure.
793
794 Proteomic analysis using LC-MS/MS: An Easy-nLC1200 chromatography system
795 (Thermo Scientific, USA) was used for peptide separation. The peptides were separated
796 using a trap (100 μm*20 mm, 5 μm, C18, Dr. Maisch GmbH) and a chromatographic
797 column (75 μm*150 mm, 3 μm, C18, Dr. Maisch GmbH) with a linear gradient of
798 buffer B (0.1% formic acid and 80% acetonitrile). The flow rate was set at 300 L/min.
799 After chromatographic separation, mass spectrometry (MS) was performed using a Q-
800 Exactive HF-X mass spectrometer (Thermo Fisher Scientific). The mass spectrometer
801 was operated in the positive ion mode and scanned from m/z 300 to 1,800 with a
802 resolution of 60,000 at m/z 200. Tandem mass spectrometry (TMS) was performed to
803 identify the 20 most intense ions. The MS data were matched against the human protein
804 database (uniProt-Homo sapiens [9606]-207393-20221227.fasta) using Proteome
805 Discoverer 2.4 (Thermo Scientific). Proteome Discoverer parameters were set as
806 follows: maximum missed cleavage sites, 2; peptide tolerance, 10 ppm; and MS/MS
807 tolerance: 0.02 Da.

808

809 **4.8 Analysis of plateletoid-induced thrombin**

810 Determination of Factor V (FV) and Factor X (FX) contents: $CaCO_3$@CSF/Ca^{2+} (0.1
811 g) was incubated with human platelet-poor plasma (400 μL, dilution factor: 2) at 25 ºC
812 for 35 min. Platelet-poor plasma supernatants were collected at predetermined time
813 points (0, 0.5, 1, 2, 3, 4, 5, 10, 15, 25, and 35 min) by centrifugation. Absorbance of
814 platelet-poor plasma was measured using UV-visible spectrophotometer (U-
815 3900010401, Hitachi, Japan). The FV and FX contents in platelet-poor plasma
816 supernatants were determined using enzyme-linked immunosorbent assay (ELISA) kits
817 (KL-FV-Pg, KL-FV-Pg, Kalang Bio, China). For comparison, $CaCO_3$/Ca^{2+} was
818 cultured with porcine platelet-poor plasma to perform the same assays following the
819 same procedure.

820

821 Thrombin activity test Thrombin activity was measured using a thrombin chromogenic
822 substrate (S-2238, S27564, Yuanye Bio, China). Initially, $CaCO_3$@CSF/Ca^{2+} (0.1 g)
823 was incubated with human platelet-poor plasma (400 μL, dilution factor: 2) at 25 ºC.
824 $CaCO_3$@CSF/Ca^{2+}-P particles were collected at predetermined times (0, 1, 2, 3, 4, 4.5,
825 5, 5.5, 6, 6.5, 7, 10, 15, 25, and 35 min), followed by freeze-drying. Next, the collected
826 particles (25 mg) were incubated with PBS (1 mL) and S-2238 solution (0.38 mg/mL,
827 1 mL) at 37 ºC. After incubation for 2 min, the reaction was immediately stopped by
828 adding acetic acid solution (50% (v/v), 1 mL). Supernatant was collected by
829 centrifugation at 5,000 rpm. Absorbance was measured at 405 nm. The thrombin

activity was determined using a thrombin calibration curve. For comparison, thrombin activity induced by $CaCO_3/Ca^{2+}$ was evaluated using the same procedure.

Procoagulant activity test Procoagulant activity was assessed using an *ex vivo* blood clotting assay. $CaCO_3$@CSF/Ca^{2+} (0.1 g) particles incubated with human platelet-poor plasma (400 μL, dilution factor: 2) at 25 ºC for predetermined time (0, 1, 2, 3, 4, 4.5, 5, 5.5, 6, 6.5, 7, 10, 15, 25, and 35 min) were collected after freeze-drying. The collected particles were added to citrated blood (2 mL), followed by the addition of $CaCl_2$ solution (0.2 M) at 37 ºC for blood clotting. The clotting times of the different samples were measured. For comparison, the procoagulant activity of thrombin induced by $CaCO_3/Ca^{2+}$ was evaluated using the same procedure.

4.9 Thrombin stability studies

Room temperature stability*:* Dry $CaCO_3$@CSF/Ca^{2+}-P was stored in a constant environment (37 ºC, 65% R.H.). At predetermined times (0, 1, 2, 3, 5, 7, 14, 21, 30, 60, and 90 days), the thrombin and procoagulant activities of $CaCO_3$@CSF/Ca^{2+}-P were tested according to the protocols described in Section 2.8. The stability of thrombin in $CaCO_3$@CSF/Ca^{2+}-T was evaluated using the same procedure.

Acidity-resistant stability: $CaCO_3$@CSF/Ca^{2+}-P particles (0.025, 0.05, 0.1, 0.2, 0.3, 0.4, 0.5, 0.7, and 1 g) were mixed with stimulated gastric fluid (10 mL) under gentle shaking at 37 ºC. After 5 min, the pH of the supernatant from the mixture was measured using

852 a pH meter (PHB-4, Inesa, China), and the thrombin and procoagulant activities of the
853 precipitates were evaluated. To study the time-dependent acidity-resistant thrombin
854 stability in $CaCO_3$@CSF/Ca^{2+}-P, 30 mg of $CaCO_3$@CSF/Ca^{2+}-P (30 mg) was mixed
855 with 10 mL of simulated gastric fluid (10 mL) for predetermined time intervals (0, 1, 3,
856 5, 7, 10, 15, 20, 30, and 60 min). The pH values of the supernatants, as well as the
857 thrombin and procoagulant activities of the precipitates from the mixture, were tested.
858 Furthermore, the pH-dependent stability of the commercial thrombin products was
859 investigated under different acidic conditions. In detail, the commercial thrombin
860 product (1 U/g, 100 μL) was mixed with simulated gastric fluid (0, 1, 2, 3, 4, 4.2, 5, and
861 10 μL), which offered the requested pH values (pH 7.34, 6.5, 6, 5.7, 5.4, 4.7, 3.5, and
862 2.3). After mixing for 5 min, the thrombin and procoagulant activities of free thrombin
863 were assessed.
864
865 **4.10 Hemostatic mechanism investigation**
866 Erythrocyte adhesion: Fresh rat blood was centrifuged at 1,200 rpm for 5 min for
867 preparation of the erythrocyte suspension. $CaCO_3$@CSF/Ca^{2+}-P (25 mg) was added into
868 of the erythrocyte suspension (5% (v/v), 500 μL), following incubation at 37 ºC for 30
869 min. The sample was washed thrice with PBS and immobilized with a glutaraldehyde
870 solution (25 mg/mL). Subsequently, ethanol dehydration of the sample was carried out.
871 After drying, the erythrocytes were imaged using SEM (SU8010, Hitachi, Japan) to
872 observe their morphology.
873

Platelet aggregation Platelets collected from rat blood were labeled with an eFluor 450-conjugated CD41a antibody (48-0411-82, Thermo Fisher Scientific, USA). 25 mg of $CaCO_3$@CSF/Ca^{2+}-P (Rh-B labeling $CaCO_3$, FITC labeling CSF) was cultured with 500 μL of the labeled platelets at 37 °C for 30 min. After washing three times with PBS, LSCM (FV3000RS, Olympus, Japan) was used to observe the aggregation status of the platelets. ImageJ software was used to quantify the fluorescence intensity of CD41a. Lactate dehydrogenase (LDH) was extracted from the platelets on $CaCO_3$@CSF/Ca^{2+}-P by lysis with Triton X-100 solution (1%). LDH in the resulting supernatant was detected using an LDH kit (A020-1-2; Nanjing Jiancheng, China). The concentration of the LDH enzyme, the quantity of platelets on $CaCO_3$@CSF/Ca^{2+}-P was obtained.

Fibrin generation: $CaCO_3$@CSF/Ca^{2+}-P (Rh-B labeling $CaCO_3$, FITC labeling CSF) (1 mg) was cultured with Alexa Fluor 350-labeled fibrinogen solution (2.5 mg/mL, 100 μL) for 5 min, before observation of the generated fibrin with LSCM (FV3000RS, Olympus, Japan). Additionally, fibrin generation was investigated based on the change in the optical density (OD) at 405 nm over time. Briefly, $CaCO_3$@CSF/Ca^{2+}-P (1 mg) was combined with fibrinogen solution (2.5 mg/mL, 100 μL) in a 96-well plate. The plate was immediately placed in a microplate reader (SYNERGY H1, BioTek, Winooski, VT, USA) to determine the total OD value within 30 min.

4.11 Ex and in vivo safety studies

Hemocompatibility evaluation: Fresh rat blood was centrifuged at 1,200 rpm for 5 min

to collect erythrocytes, followed by washing with PBS for 3 times. $CaCO_3$@CSF/Ca^{2+}-P solutions (0.5, 1, 5, and 10 mg/mL) were mixed with PBS (3 mL) and erythrocytes (60 μL). After incubation at 37 ºC for 1 h, the supernatant was collected by centrifugation at 1,200 rpm for 5 min. Haemolysis was calculated as described previously.

Cytocompatibility evaluation: Murine fibroblast cells (L929) were used to evaluate cytocompatibility. UV-sterilized $CaCO_3$@CSF/Ca^{2+}-P (0.1 g/mL) was directly soaked in Dulbecco's modified Eagle's medium (DMEM) at 37 ºC for 24 h to acquire the extract of $CaCO_3$@CSF/Ca^{2+}-P. The obtained extract was introduced into a 96-well plate containing cells that had been seeded at a density of 10^4 cells/well. Cytotoxicity was assessed using the Cell Counting Kit-8 (CCK8; BS350B, Biosharp, China) after incubation for different times (24, 48, and 72 h). A live/dead double staining kit (Calcein-AM/PI, 40747ES76, Yeasen, China) was used to evaluate the effect of the extract of $CaCO_3$@CSF/Ca^{2+}-P on the cells. Untreated L929 cells served as blank controls.

In vivo toxicity assay: To assess the toxicity of $CaCO_3$@CSF/Ca^{2+}-P *in vivo*, rats (n = 3) were administered with $CaCO_3$@CSF/Ca^{2+}-P orally for 7 days. Rats were weighed daily during the 7 d trial. On day 8, after blood collection for biochemical analysis, all rats were euthanized. Next, the gastrointestinal tract and vital organs (the heart, liver, spleen, lungs, and kidneys) were collected for histological analysis. Furthermore,

calcium accumulation in the major organs was measured. Rats (n = 3) orally administered with PBS were used as blank controls.

4.12 Hemostasis in gastric mucous

Acidity regulation in stomach: Rats (n = 3) were administered with $CaCO_3$@CSF/Ca^{2+}-P (0, 10, 20, 30, 50, 70 and 100 mg) orally, and sacrificed to collect their stomachs. The acidity of the gastric fluid was measured. Time-dependent acquisition (at 0, 3, 5, 10, 30, 60, 120, and 180 min) in the stomach followed a similar approach, except that the dose of $CaCO_3$@CSF/Ca^{2+}-P was 30 mg.

Hemostasis: Rats (n = 9) were fasted for 24 h before conducting the experiments while still being able to freely access water. To induce acute gastric ulcer bleeding, rats received an oral ethanol-HCl mixed solution (0.6 M HCl in absolute ethanol) (0.01 mL/g). After 10 min, the rats with acute gastric ulcer bleeding were randomly assigned to three groups: Group 1, administered PBS (1 mL); Group 2, administered the $CaCO_3$@CSF/Ca^{2+}-P dispersion (30 mg/mL, 1 mL); and Group 3, without treatment. Subsequently, the rats were provided access to food and water. Fresh fecal samples were collected daily for the fecal occult blood assay using an assay kit (O-toluidine method, JLC0144, Jingkang Bio, China). Furthermore, a rat fecal occult blood ELISA kit (JLC7418, Jingkang Bio, China) and Rat TRF ELISA kit (JLC4154, Jingkang Bio, China) were used to determine the concentrations of ferroheme and transferrin in the feces.

940

941 Distribution of $CaCO_3$@CSF/Ca^{2+}-P in gastric tissues Upon oral administration of PBS
942 or $CaCO_3$@CSF/Ca^{2+}-P (FITC labeling CSF), rats (n = 3) with acute gastric ulcer
943 bleeding for 30 min, were euthanized to collect gastric tissues. The gastric tissues were
944 then opened along the greater curvature and washed with PBS. The gastric tissues were
945 stretched out to capture images and imaged by an IVIS Lumina In Vivo Imaging System
946 (IVIS Lumina Series III10899, PerkinElmer, USA). Thereafter, the gastric tissues were
947 stained with hematoxylin (and) for histological analysis.

948

949 Immunofluorescence staining: Platelet-specific marker, CD41, was used to track
950 platelet plugs in hemostatic clots from the injured gastric tissue. The staining involved
951 the use of a CD41 Antibody (PA5-79527, Thermo Fisher Scientific, USA) and a Goat
952 anti-Rabbit IgG (H+L) Cross-Adsorbed Secondary Antibody, Alexa Fluor™ 568 (A-
953 11-11, Thermo Fisher Scientific, USA). The paraffin sections of the gastric tissues were
954 deparaffinized and rehydrated. Antigen retrieval buffer (EDTA, pH 9.0, 1:50 dilution
955 of 1:50) was used to retrieve antigens in the sections with microwave assistance.
956 Nonspecific binding sites were blocked by incubating the sections with 10% of sheep
957 serum for 40 min. These sections were incubated with the CD41 primary antibody
958 (dilution factor: 200) at 4 °C overnight, followed by incubation with the secondary
959 antibody (dilution factor: 200). After staining the sections with DAPI (4',6-diamidino-
960 2-phenylindole, R20278, Yuanye Bio, China) (dilution factor: 1,000),
961 immunofluorescence images of the sections were captured by a Vectra Polaris

Automated Quantitative Pathology Imaging System (PerkinElmer, USA). ImageJ J was employed to analyze the CD41 staining semi-quantitatively analyze CD41 staining.

4.13 Statistical analysis

Statistical analyses were performed using GraphPad Prism 8. Data were analyzed using the Student's unpaired *t*-test, one-way analysis of variance (ANOVA), or two-way ANOVA. Results are expressed as means ± standard deviation. Statistical significance was set at $*P < 0.05$, $**P < 0.01$, $***P < 0.001$, and $****P < 0.0001$.

Conflicts of interest

There are no conflicts of interest to declare.

Acknowledgments

This work was supported by the National Natural Science Foundation of China (No. 52103096), Fundamental Research Funds for the Central Universities (grant number SWU-KT22004), and Ernst Mach Grant Scholarship (financed by the Austrian Federal Ministry of Education, Science and Research, No. MPC-2022-04099).

References

[1] a)S. Li, Y. Zhang, S.-H. Ho, B. Li, M. Wang, X. Deng, N. Yang, G. Liu, Z. Lu, J. Xu, Q. Shi, J.-Y. Han, L. Zhang, Y. Wu, Y. Zhao, G. Nie, *Nature Biomedical Engineering* **2020**, 4, 732; b)F. I. Üstok, J. A. Huntington, *Blood* **2022**, 139, 2972.

[2] A. Girish, K. Jolly, N. Alsaadi, M. de la Fuente, A. Recchione, R. An, D. Disharoon, Z. Secunda, S. Raghunathan, N. F. Luc, C. Desai, E. Knauss, X. Han, K. Hu, H. Wang, U. D. S. Sekhon, N. Rohner, U. A. Gurkan, M. Nieman, M. D. Neal, A. Sen Gupta, *ACS Nano* **2022**, 16, 16292.

[3] B. Zhuang, Z. Li, J. Pang, W. Li, P. Huang, J. Wang, Y. Zhou, Q. Lin, Q. Zhou, X. Ye, H. Ye, Y. Liu, L. M. Zhang, R. Chen, *Int J Nanomedicine* **2015**, 10, 939.
[4] S. Bianco, M. Hasan, A. Ahmad, S.-J. Richards, B. Dietrich, M. Wallace, Q. Tang, A. J. Smith, M. I. Gibson, D. J. Adams, *Nature* **2024**, 631, 544.
[5] a)Y. Wu, Z. Song, G. Deng, K. Jiang, H. Wang, X. Zhang, H. Han, *Small* **2021**, 17; b)K. Liu, Q. Liu, J. Yang, C. Xie, S. Wang, F. Tong, J. Gao, L. Liu, Y. Ye, B. Chen, X. Cai, Z. Liu, Z. Li, F. Peng, Y. Tu, *ACS Nano* **2022**, 17, 300.
[6] A. L. Lira, R. S. Ferreira, M. L. V. Oliva, A. A. Sousa, *Langmuir* **2020**, 36, 7991.
[7] a)X. Lu, P. Xu, H.-M. Ding, Y.-S. Yu, D. Huo, Y.-Q. Ma, *Nature Communications* **2019**, 10; b)M.-E. Mäeots, B. Lee, A. Nans, S.-G. Jeong, M. M. N. Esfahani, S. Ding, D. J. Smith, C.-S. Lee, S. S. Lee, M. Peter, R. I. Enchev, *Nature Communications* **2020**, 11.
[8] a)A. S. Khalil, X. Yu, J. M. Umhoefer, C. S. Chamberlain, L. A. Wildenauer, G. M. Diarra, T. A. Hacker, W. L. Murphy, *Science Advances* **2020**, 6, eaba2422; b)L. Zhou, K. Yu, F. Lu, G. Lan, F. Dai, S. Shang, E. Hu, *Journal of Cleaner Production* **2020**, 243.
[9] A. S. Wolberg, R. A. Campbell, *Transfusion and Apheresis Science* **2008**, 38, 15.
[10] U. D. S. Sekhon, K. Swingle, A. Girish, N. Luc, M. de la Fuente, J. Alvikas, S. Haldeman, A. Hassoune, K. Shah, Y. Kim, S. Eppell, J. Capadona, A. Shoffstall, M. D. Neal, W. Li, M. Nieman, A. Sen Gupta, *Science Translational Medicine* **2022**, 14, eabb8975.
[11] J.-P. Motta, A. Denadai-Souza, D. Sagnat, L. Guiraud, A. Edir, C. Bonnart, M. Sebbag, P. Rousset, A. Lapeyre, C. Seguy, N. Mathurine-Thomas, H. J. Galipeau, D. Bonnet, L. Alric, A. G. Buret, J. L. Wallace, A. Dufour, E. F. Verdu, M. D. Hollenberg, E. Oswald, M. Serino, C. Deraison, N. Vergnolle, *Nature Communications* **2019**, 10.
[12] a)B. R. Lentz, *Progress in Lipid Research* **2003**, 42, 423; b)E. C. Reddy, M. L. Rand, *Frontiers in Cardiovascular Medicine* **2020**, 7.
[13] E. A. Ruben, B. Summers, M. J. Rau, J. A. J. Fitzpatrick, E. Di Cera, *Blood* **2022**, 139, 3463.
[14] X. Shang, H. Chen, V. Castagnola, K. Liu, L. Boselli, V. Petseva, L. Yu, L. Xiao, M. He, F. Wang, K. A. Dawson, J. Fan, *Nature Catalysis* **2021**, 4, 607.
[15] Z. Lu, S. Du, J. Li, M. Zhang, H. Nie, X. Zhou, F. Li, X. Wei, J. Wang, F. Liu, C. He, G. Yang, Z. Gu, *Advanced Materials* **2023**, 35, 2303388.
[16] N. Drenchev, O. Lagunov, K. Hadjiivanov, *Microporous and Mesoporous Materials* **2023**, 362.
[17] a)G. Steiner, S. Tunc, M. Maitz, R. Salzer, *Analytical Chemistry* **2007**, 79, 1311; b)H. C. Davis, N. D. Posey, G. N. Tew, *Biomacromolecules* **2022**, 23, 57.
[18] M. Mahmoudi, M. P. Landry, A. Moore, R. Coreas, *Nature Reviews Materials* **2023**, 8, 422.
[19] A. Shukla, J. C. Fang, S. Puranam, F. R. Jensen, P. T. Hammond, *Advanced Materials* **2011**, 24, 492.
[20] Z. Liu, L. Xiang, M. Tian, H. Wang, X. Zhao, K. Liu, J. Yu, T. Liu, S. Liu, X. Mu, B. Yang, S. Zhang, J. Luo, *Advanced Materials* **2023**, 35.
[21] Q. Xiao, M. Zoulikha, M. Qiu, C. Teng, C. Lin, X. Li, M. A. Sallam, Q. Xu, W. He, *Advanced Drug Delivery Reviews* **2022**, 186.
[22] S. Gou, W. Geng, Y. Zou, F. Chen, T. He, Q. Duan, Z. Qin, L. Li, J. Xia, Y. Yu, Q. Feng, K. Cai, *ACS Nano* **2024**, 18, 9871.
[23] Z. Hu, S. Yan, X. Li, R. You, Q. Zhang, D. L. Kaplan, *ACS Nano* **2021**, 15, 8171.
[24] a)C. Yang, S. Shang, D. Shou, L. Ran, G. Lan, E. Hu, *Journal of Cleaner Production* **2021**, 314, 127996; b)L. Xiong, H. Wang, J. Wang, J. Luo, R. Xie, F. Lu, G. Lan, L.-J. Ning, R. Yin, W. Wang, E. Hu, *ACS Applied Materials & Interfaces* **2023**, 15, 49035; c)Y. Wang, P. Guan, R. Tan, Z. Shi, Q. Li, B. Lu, E. Hu, W. Ding, W.

Wang, B. Cheng, G. Lan, F. Lu, *Advanced Fiber Materials* **2024**.
[25] Y.-Q. Niu, J.-H. Liu, C. Aymonier, S. Fermani, D. Kralj, G. Falini, C.-H. Zhou, *Chemical Society Reviews* **2022**, 51, 7883.
[26] a)H. Qiu, L. Gong, P. Slezak, S. He, F. Lu, K. Yu, J. Xie, Z. Geng, E. Hu, Z. Zhou, G. Lan, R. Xie, *International Journal of Biological Macromolecules* **2024**, 275, 133584; b)G. Zhou, F. Lu, S. Shang, D. Shou, W. Wang, K. Yu, R. Xie, G. Lan, E. Hu, *Journal of Materials Chemistry B* **2023**, 11, 3885; c)Y. Ye, Z. Chen, S. Zhang, P. Slezak, F. Lu, R. Xie, D. Lee, G. Lan, E. Hu, *Research* **2024**, 7, 0388; d)H. Qiu, G. Lan, W. Ding, X. Wang, W. Wang, D. Shou, F. Lu, E. Hu, K. Yu, S. Shang, R. Xie, *Research* **2022**, 2022; e)C. Yuan, Y. Ye, E. Hu, R. Xie, B. Lu, K. Yu, W. Ding, W. Wang, G. Lan, F. Lu, *Carbohydrate Polymers* **2024**, 334, 122058; f)Z. Chen, C. Yuan, Y. Ye, B. Lu, E. Hu, F. Lu, K. Yu, R. Xie, G. Lan, *Carbohydrate Polymers* **2024**, 328, 121703.
[27] X. Zhang, L. Xiao, Z. Ding, Q. Lu, D. L. Kaplan, *ACS Nano* **2022**, 16, 10209.
[28] S. Handtke, T. Thiele, *Journal of Thrombosis and Haemostasis* **2020**, 18, 1256.
[29] A. S. Wolberg, *Blood Reviews* **2007**, 21, 131.
[30] X. Li, L. Yuan, D. Liu, M. Liao, J. Chen, K. Yuan, J. Xiang, Z. Li, Y. Huang, *Advanced Functional Materials* **2021**, 31.
[31] H. Y. Chung, Y. Bian, K.-M. Lim, B. S. Kim, S. H. Choi, *Nature Communications* **2022**, 13.
[32] B. Wang, R. Zheng, W. Yang, X. Han, C. Hou, Q. Zhang, Y. Li, K. Li, H. Wang, *Advanced Functional Materials* **2022**, 32.
[33] J. M. Antosiewicz, D. Shugar, *Biophysical Reviews* **2016**, 8, 163.
[34] M. Ndonwi, E. A. Tuley, G. J. Broze, *Blood* **2010**, 116, 1344.
[35] K. J. Kearney, J. Butler, O. M. Posada, C. Wilson, S. Heal, M. Ali, L. Hardy, J. Ahnström, D. Gailani, R. Foster, E. Hethershaw, C. Longstaff, H. Philippou, *Proceedings of the National Academy of Sciences* **2021**, 118.
[36] R. Majumder, M. A. Quinn-Allen, W. H. Kane, B. R. Lentz, *Blood* **2008**, 112, 2795.
[37] N. Pozzi, Z. Chen, L. A. Pelc, D. B. Shropshire, E. Di Cera, *Proceedings of the National Academy of Sciences* **2014**, 111, 7630.
[38] Q. Lu, L. Yang, C. Manithody, X. Wang, A. R. Rezaie, *Thrombosis Research* **2014**, 134, 1103.
[39] J. A. Huntington, *Biochimica et Biophysica Acta (BBA) - Proteins and Proteomics* **2012**, 1824, 246.
[40] Y. Xie, J. An, G. Yang, G. Wu, Y. Zhang, L. Cui, Y. Feng, *Journal of Biological Chemistry* **2014**, 289, 7994.
[41] G. R. R. Martin, *A Game of Thrones 4-Book Bundle: A Song of Ice and Fire Series: A Game of Thrones, A Clash of Kings, A Storm of Swords, and A Feast for Crows*, Random House Publishing Group, **2011**.
[42] X. Shang, H. Chen, Y. Qu, J. Fan, *RSC Advances* **2016**, 6, 3458.
[43] C. Xuan, L. Hao, X. Liu, Y. Zhu, H. Yang, Y. Ren, L. Wang, T. Fujie, H. Wu, Y. Chen, X. Shi, C. Mao, *Biomaterials* **2020**, 252.
[44] Y. Liu, K. Yu, S. Shang, R. Xie, F. Lu, R. Bao, G. Lan, E. Hu, *Nanoscale* **2021**, 13, 9843.
[45] B. Estevez, K. Kim, M. K. Delaney, A. Stojanovic-Terpo, B. Shen, C. Ruan, J. Cho, Z. M. Ruggeri, X. Du, *Blood* **2016**, 127, 626.
[46] D. Butera, P. J. Hogg, *Nature Communications* **2020**, 11.
[47] P. Huang, L. Jiang, H. Pan, L.-W. Ding, B. Zhou, M. Zhao, J. Zou, B. Li, M. Qi, H. Deng, Y. Zhou, X. Chen, *Advanced Materials* **2022**, 35.
[48] D. Xu, Y. Zhu, M. Su, J. Chen, S. Shen, C. F. Xu, X. Yang, *Advanced Functional Materials* **2023**, 33.
[49] J. W. O'Brien, M. Rogers, M. Gallagher, T. Rockall, *Surgery* **2022**, 40, 582.
[50] a)S. Tanabe, *Digestive Endoscopy* **2021**, 34, 61; b)Z. Yang, L. Chen, J. Liu, H. Zhuang, W. Lin, C. Li, X.

Zhao, *Adv Mater* **2023**, 35, e2301849.
[51] J. J. Y. Sung, L. Laine, E. J. Kuipers, A. N. Barkun, *Gut* **2021**, 70, 818.
[52] a)A. Lanas, J.-M. Dumonceau, R. H. Hunt, M. Fujishiro, J. M. Scheiman, I. M. Gralnek, H. E. Campbell, A. Rostom, C. Villanueva, J. J. Y. Sung, *Nature Reviews Disease Primers* **2018**, 4; b)J. Molina-Infante, M. Fernandez-Bermejo, G. Vinagre-Rodríguez, *Endoscopy* **2011**, 43, E191.
[53] C. Zhao, G. Chen, H. Wang, Y. Zhao, R. Chai, *Bioactive Materials* **2021**, 6, 1653.
[54] C. E. Hansen, D. R. Myers, W. H. Baldwin, Y. Sakurai, S. L. Meeks, L. A. Lyon, W. A. Lam, *ACS Nano* **2017**, 11, 5579.
[55] L. Shan, J. Wang, H. Tu, W. Zhang, H. Li, P. Slezak, F. Lu, D. Lee, E. Hu, Z. Geng, G. Lan, R. Xie, *Carbohydrate Polymers* **2024**, 343, 122505.